Transport and Decoherence Phenomena in Quantum Dots

by

Kai Xi Wang

A thesis
presented to the University of Waterloo
in fulfillment of the
thesis requirement for the degree of
Master of Applied Science
in
Electrical and Computer Engineering (Nanotechnology)

Waterloo, Ontario, Canada, 2020

Author's Declaration

This thesis consists of material all of which I authored or co-authored: see Statement of Contributions included in the thesis. This is a true copy of the thesis, including any required final revisions, as accepted by my examiners.

I understand that my thesis may be made electronically available to the public.

Statement of Contributions

This thesis consists of two projects – one on interband transitions in QD, and the other on intersublevel transitions. The interband material may be used in a future publication. The interband quantum dot project was performed with collaborators, under Prof. Dayan Ban's supervision. Experimental linewidth broadening data were provided by Dr. Sofiane Haffouz, Dr. Dan Dalacu, and Dr. Philip Poole at the National Research Council in Ottawa. Dr. Rassel Shazzard provided Figure 3.2 in this thesis (which is a schematic of the structure under study), as well as editorial inputs. The theoretical and computational results, and the written work are produced by myself, with technical and scientific feedback as well as minor adjustments from Prof. Stephen Hughes. Prof. Stephen Hughes also provided feedback for the quantum dot cascade laser section of this thesis, which has been presented as a poster, at the 2019 Infrared Terahertz Quantum Workshop (ITQW).

Abstract

The problem of a few electronic level coupling to an environmental heat bath, such as in quantum dots (QDs), is well-known in modern quantum physics. These systems have been widely studied as they can dictate the dephasing properties in many practical opto-electronic devices. In this thesis we focus on the electron-phonon (quantized lattice vibrations) coupling in QDs that are embedded within semiconductor nanowires.

For interband optical transitions, the electron-phonon interactions are treated using a cumulant expansion approach which includes the non-Markovian dynamics. Both the longitudinal optical (LO) and longitudinal acoustic (LA) phonons are included, and structural variations of the QDs are investigated, which, typically the LO phonons and structural asymmetry have been neglected in the literature. We find that the linewidth can have variations on three orders of magnitude when changing the QD geometry due to LO phonon interactions, which obviously has significant implications in mitigating phonon-induced dephasing. Comparison to experimental results is shown for validation of the theoretical model. Finally, we elucidate these effects for single photon emitters composed of different materials.

In the intersublevel regime, we study the electron transport dynamics in a quantum dot cascade laser (QDCL), which is a promising candidate as the semiconductor gain medium for THz lasing. The quantum kinetics are included by means of an intuitive and accurate density matrix approach, valid for weak to intermediate e-phonon interaction strength. We find that at low temperatures, the LA phonons can help to inject electrons into the upper lasing state.

We believe these findings should be considered and utilized in future opto-electronic device designs.

Acknowledgements

First and foremost I am deeply indebted to my supervisor Professor Dayan Ban, for all the support and mentorship, wisdom and kindness, starting all the way from my undergraduate studies. I would also like to thank Dr. Seyed Ghasem Razavipour, for getting me started in THz QCL simulations.

I owe my deepest gratitude to Professor Hughes, for teaching me the ways of theoretical physics research, for putting up with my stupid mistakes, and quickly responding to my emails and answering my questions. I would also like to thank his student Chris Gustin, for sharing his code.

My deepest gratitude goes to my collaborators. This includes Dr. Sofiane Haffouz, Dr. Dan Dalacu, and Dr. Philip Poole at the National Research Council, who had provided their PL data on the QD in nanowire sample. I also thank Dr. Shazzad Rassel for his editorial and scientific inputs in this project. I would like to thank Andrew Pan who took the time to respond to my emails about the scattering superoperator, and along with Benjamin Burnett, generously provided notes on the periodicity of the scattering superoperator. Without everyone's help this thesis would not have been possible!

It was also a pleasure to work with Dr. Emmanuel Dupont at the National Research Council in Ottawa. I learned a lot during the 4 months while I was there, and I express my sincere gratitude for setting up the opportunity and sharing your work!

I am in debt to Chris Deimert and Prof. Wasilewski, who have provided the THz QCL growths, as well as Chao and Siyi for their fabrication and experimental help. I also thank Chao for being a great office mate and friend. I thank Jian for sharing his research experience and answering my questions regarding the MASc degree completion process. I am also grateful for the THz QCL collaborations with Boyu. My thanks also goes to Zhongda Zhang for his experimental help, and Xiaoliang, Yue, Burak as well as all the current and past members of Prof. Dayan Ban's group.

I am very grateful towards Professor Wilson and Professor Bajcsy who agreed to be the readers of this thesis. I also thank Zoe Tipper, the MASc coordinator/advisor for all her help in the MASc degree completion process.

I am thankful for all the co-op research experiences that I have had during my undergraduate career – especially to Prof. Sun's group and Qian Sun who had patiently provided me with close mentorship and got me started in research, as well as Lynna Chen for the opportunity at MIT.

I would also like to thank my highschool physics teacher John Berrigan who initiated my interest in physics.

Last but not least, I thank my family and friends, and Theo for all the love, encouragement, care, support, (and nagging) as I finish this thesis.

Dedication

Dedicated to family, friends, and mentors.

Table of Contents

List of Tables

List of Figures

Chapter 1

Introduction

1.1 Quantum Dots

Progress in nanofabrication techniques of low-dimensional semiconductor materials in the past few decades have opened up opportunities for their fundamental research and applications. Starting around the 1970's, development of Metalorganic vapour-phase epitaxy and Molecular Beam Epitaxy techniques enabled the quantum confinement scenarios in textbooks to be experimentally realized. This brought on a whole new era of bandgap engineering and novel optoelectronic devices. Semiconductor quantum wells, which are formed when materials of different bandgaps are layered together, results in the spatial quantum confinement in one direction. These can be used in laser diodes which have higher radiative efficiency than their bulk counterpart. Esaki and Tsu presented analysis on the transport properties of quantum well superlattices [1, 2], which had now lead to the advent of quantum cascade lasers. These are lasers emitting in the THz (10^{12} Hz) region of the electromagnetic spectrum.

In the 1980's, researchers naturally investigated the further reduction of dimensionality – synthesizing quantum dots (QDs). QDs are small regions of semiconductor materials, typically 2-100nm in size (see Figure 1.1 a). They can be embedded within a different material, or dispersed in a different medium. The different band-gaps of the materials result in spatial confinement of the charge carriers (electrons and holes) in all three dimensions. First direct evidence demonstrating the 3-dimensional spatial confinement in QDs was by Reed et al in 1986 [3]. Soon reports from other groups followed. The quantum confinement results in discrete energy levels, and they share similar properties to atomic levels – such

as optical selection rules, spd shells, etc., hence the name artificial atoms (see Figure 1.1 b).

Electrons in QDs can be excited from the valence band to the conduction band, leaving holes in the valence band. The electron and hole then bind via the Coulomb attraction, to form the electron-hole pair. If the interaction is strong enough, then a new charge carrier the exciton is formed.

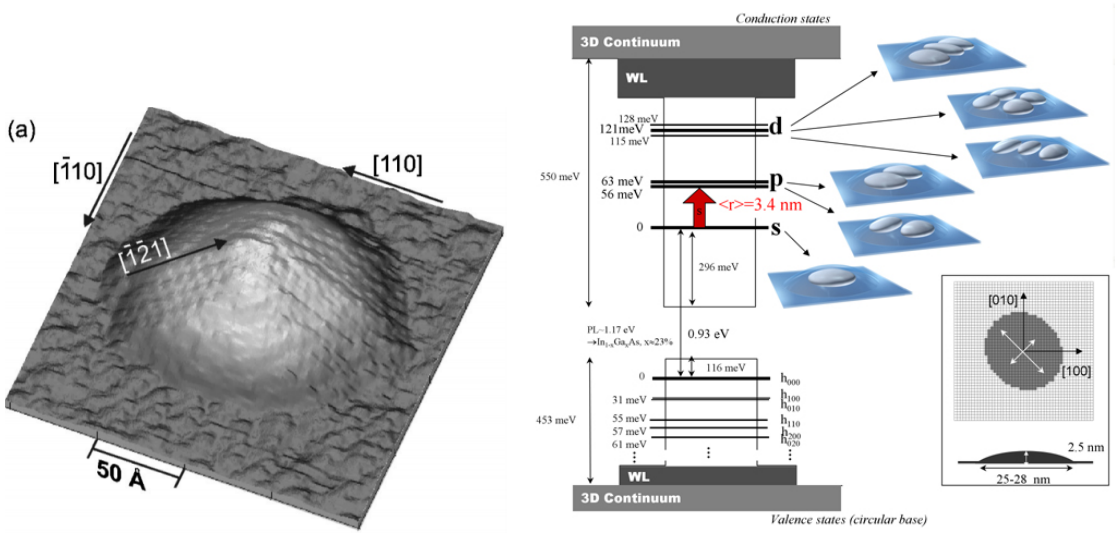

Figure 1.1: a) STM image of an InAs QD, reproduced from [4] b) Level diagram of a QD, showing the spd levels and the associated wavefunctions, reproduced from [5]

One popular way to make quantum dots is using the (self-assembled) Stranski-Kransanov method. In this method a layer of material is deposited on another substrate using molecular beam epitaxy. The lattice mismatch of the different materials cause strain resulting in QDs to form in random positions. Afterwards, another layer of material can be grown on top.

For better control of size, geometry, and location of the QD, high quality single QDs can be grown, bottom up, within nanowires (see Figure 1.2). One way to do this is to use a metal catalyst particle combined with selective-area and Vapour-Liquid-Solid process. The QD diameter is dictated by the size of the metal catalyst particle, and the QD is incorporated into the nanowire by simply switching the precursor gases during the nanowire growth.

The nanowire geometry has several advantages – the nanowire itself also acts as a

waveguide, resulting in control of the emission direction, spontaneous emission rate, and high extraction efficiencies. These structures also provide the possibilities for surface coatings, reducing surface charge noise, which are due to the random trapping and de-trapping of charges at the nanowire surface. However, even with coatings these QD in nanowires structures are still fundamentally limited by the phonon decoherence – which is one of the topics of study in this thesis.

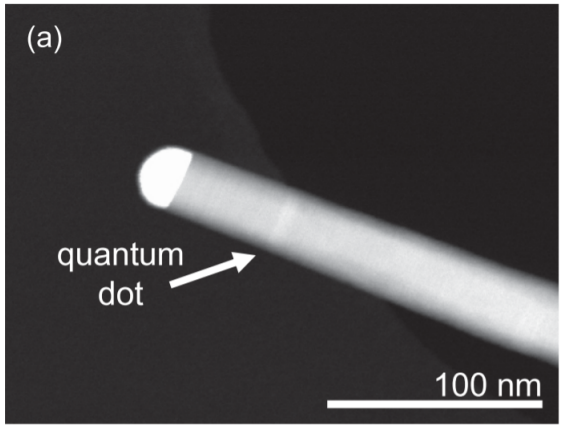

Figure 1.2: TEM image of a QD in nanowire from [6]

These QD in nanowire structures have applications in many quantum technologies such as lasers, photodetectors, and single photon emitters. Single photon emitters in particular have applications in quantum key distributions. This requires that the probability of emitting multiple photons are negligible, as well as being indistinguishable. In this regard, understanding and engineering the optical emission properties is of crucial importance.

One of the main factors in determining the optical lineshape, at low temperatures, are phonons. Phonon decoherence is present even at 0K and presents a fundamental limit. It is well known that the optical lineshape for interband transitions in QDs follow an overall non-Lorentzian spectrum, and this is different from its atomic analogue. There are broad sidebands due to interactions with low energy (LA) phonons, which is superimposed on a narrow Lorentzian zero phonon line (ZPL) – see Figure 1.3. This means that in the time domain, the photoluminescence signal exhibits at short times scale a fast initial non-exponential decay, followed by at longer time scales a slow exponential decay. For higher temperatures these features become smeared out, with many other different processes contributing to the linewidth broadening as well.

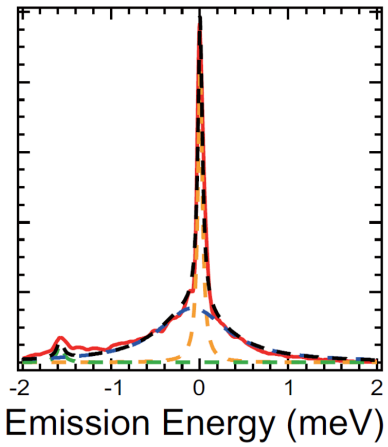

Figure 1.3: A typical emission spectrum of InAs self-assembled QDs, broadened due to interactions with LA phonons, reproduced from [7]

Early work to include phonon interactions in the emission spectrum include independent boson models (IBM)[8, 9], which well accounts for the broad LA phonon sidebands. However this had the issue of a residual coherence in the polarization and hence exhibited an infinitely narrow ZPL. Mechanisms accounting for the broadening of the ZPL due to phonons include taking account virtual transitions or 2 phonon interactions [10, 11, 12], different dimensionality of the LA phonon modes [13, 14], and taking into account a finite phonon lifetime due to scattering from interfaces [15, 16] or reservoir anharmonicity [17]. Approaches extending the IBM, such as correlation expansion [18] and the polaron master equation approach [19, 20, 21, 22] can also account for ZPL broadening associated with other effects, such as radiative decay and pump induced broadening, as well as the implementation of coherent driving which ultimately is needed to understand limits of pulse-generated single photons [23]. Still, frequently the broadening of the ZPL due to phonons have been included phenomenologically or with some fit function linearly proportional to the temperature [24], although recently more detailed schemes have been developed in Refs. [25, 26]. The seminal work by Muljarov et al [11] had included a second order perturbation term to address the broadening of the ZPL, but the full solution relies on a Fredholm integral eigen value problem. Recently [14] showed that inclusion up to the second order in this term is a good approximation of the full solution, however no experimental comparison is shown. For indistinguishable single photon sources the value of the ZPL linewidth is even more crucial since the broad sidebands can be filtered out [27]. Other relevant recent studies on the ZPL broadening include [7, 28, 29], however the theoretical analysis of the ZPL broadening due to phonons was not included. Therefore

fundamental studies solely comparing the experimental and theoretical emission spectra of single QDs without other processes are needed for a careful evaluation of the linewidth broadening.

Similar phenomenology have also been suggested for the intersublevel lineshape [30]. In this frequency regime (roughly 0.3-10THz or 30-1000um wavelength), one major area of research is in the design of an ideal room temperature THz emitter [31]. Candidate material systems include QDs, which have been proposed to serve as building blocks for quantum dot cascade lasers (QDCLs). These are analogous to the traditional quantum-well based quantum cascade lasers [32, 33], which operate based on intersubband transitions, but with additional lateral quantum confinement. Although room temperature lasing has been predicted in previous theoretical works [34, 35], its experimental realization at room temperature has yet to be achieved. Nevertheless, practical routes utilizing top-down etching schemes [36, 37] have been successfully demonstrated. However, significant practical challenges exist, such as leakage currents due to the presence of surface charges and the low fill factor of the gain material. On the theoretical side, detailed but also intuitive modeling schemes have not been well established either. In this thesis density matrix based model is proposed to simulate for its operation characteristics.

1.2 Overview of thesis

This thesis consists of five chapters. Chapter 1 has introduced the topics covered in this thesis. Chapter 2 presents foundational background material which are to be used in the rest of this thesis. The basis or wavefunctions that are used for QD in nanowire structures is explained, followed by the derivation of the Hamiltonians describing the interactions of those states with the environment (photons and phonons). Basic transport formalisms are reviewed. All the important equations are highlighted in boxes.

Chapter 3 explains the theoretical work on the spectral broadening of interband QD transitions due to interactions with LA and LO phonons. Both the linear and quadratic coupling terms are included. Comparison to the experimental results, and structural and material variations are made. In contrast to the present literature, this work has several contributions.

- The cylindrical basis is used in this work which is physically more similar to the shape of typical QDs, while in most of the literature Gaussian spherical wavefunctions are used.

- The wavefunction calculation method in this thesis is also applicable to any arbitrary potential variation in the radial direction, as well as in the growth direction.
- The LO phonon virtual interaction is included along with the LA phonons using the cumulant expansion approach. Although the theory for the quadratic interaction for LA and LO phonons is not new, it has not been implemented using wavefunctions in a cylindrical basis before.
- Direct comparison to experimental data with single QDs in nanowires are made.

Chapter 4 presents the theoretical modelling done for an application in the intersublevel regime – namely quantum dot cascade lasers, which are promising as the gain material for emission in the THz regime. The model is a type of Redfield or otherwise also know as Interaction transport model. Although the density matrix transport theories and the Interaction approach are not new, this has never been applied to QDCLs before. Finally, conclusions and possible future directions are presented in Chapter 5.

All the codes used to generate the results in this thesis are written in MATLAB, the main codes will be provided on Github: https://github.com/kx-wang.

Chapter 2

Fundamentals

This section reviews and derives some fundamental background necessary for the remainder of this thesis. They are of interest / importance to those working in the fields of semiconductor quantum physics. Generally in quantum mechanics, there are two questions of interest – what states there are, and how those states interact. I define the bandstructure or basis used, derive the interaction Hamiltonians of the QD states with the environment (phonons and photons), and review the quantum equations of motion.

2.1 Wavefunctions

In order to understand the transport properties of carriers in QDs, one needs to first find the quantum states. There are different possible ways to calculate the wavefunctions of quantum dots – such as $k \cdot p$ [38], and tight binding [39] approaches. Although the accurate modelling of the bandstructure in QDs requires those methods, here the envelope function and effective mass approximations are used, because it is simple to employ and allows for fast exploration of the geometric and materials design space.

Under the envelope function approach, it is assumed that the total wavefunction for the electrons in the conduction band (c), or holes in the valence band (v) is given by $\Phi^{c/v}(\mathbf{r}) = \sum_n \psi_n^{c/v}(\mathbf{r}) u_{nk}^{c/v}(\mathbf{r})$, where u is the periodic Bloch functions due to the atomic potential, $\psi_n^{c/v}$ is the slowly varying envelope function arising from quantum confinement on the nanoscale, k is the wavevector, and r is the spatial coordinate. The sum over n denotes the sum over the contributions of the other bands to the target one – for example the conduction band is affected by contributions from the valence bands.

For direct bandgap, the expansion of the Bloch function can be taken around the Γ point (k=0),

$$u_{mk} = \sum_n c_n(k) u_{n0} \tag{2.1}$$

Substitution of this into the time independent Schrödinger equation yields the effective envelope Schrödinger equation [40],

$$\sum_m [H_{nm}(-i\hbar\nabla) + V(r)]\psi_m^{c/v}(r) = E\psi_n^{c/v}(r) \tag{2.2}$$

Restricting to an effective one band, which is assuming that the conduction band wavefunctions are predominantly of conduction band character (the contribution of light-hole/heavy-hole/split-off bands are small enough), and the valence band wavefunctions can be modeled by one effective valence band. Adding the effect of the Coulomb attraction, finally the single particle Hamiltonian is given by [41]

$$H = \sum_{i=c,v} -\frac{\hbar^2\nabla^2}{2m_i} + U_i(r) + \frac{q_1 q_2 \psi_e(r)\psi_h(r)\psi_h(r)\psi_e(r)}{4\pi\epsilon|r_e - r_h|} dr dr' \tag{2.3}$$

where $U_i(r)$ is the confinement potential from the conduction/valence band offsets, and the third term is due to the Coulombic attraction between the electrons and holes. Now if assuming the strong confinement regime, the Coulombic term can be ignored.

As mentioned in Chapter 1, the geometry under study in this thesis are QDs in nanowires. For the InAs QDs that are compared to experimental results in Chapter 3, the Bohr radius of bulk InAs is 34nm [42] while the radius/height of our QD is 9nm/5nm, and hence the Coulombic term can be ignored. The QDs take on a disk-like shape, and to model this type of system, it is natural to start by writing the Schrödinger equation in cylindrical coordinates

$$H(z) = \frac{-\hbar^2}{2}\left(\frac{\partial}{\partial z}\frac{1}{m_{c,v}^z}\frac{\partial}{\partial z}\right) + V_{c,v}(z) \tag{2.4}$$

$$H(r,\theta) = \frac{-\hbar^2}{2}\left(\frac{1}{r}\frac{\partial}{\partial r}\left(r\frac{1}{m_{c,v}^r}\frac{\partial}{\partial r}\right) + \frac{1}{m_{c,v}^r}\frac{1}{r^2}\frac{\partial^2}{\partial\theta^2}\right) + V_{c,v}(r,\theta) \tag{2.5}$$

where $m_{c,v}^z$ and $m_{c,v}^r$ are the effective masses of electrons or holes in the z and in plane directions respectively - z is along the axis of the nanowire. Since the total potential can be separated into the sum of the radial and z components, the separation of variables can be used and the envelope wavefunctions are factorized to be

Wavefunctions

$$\psi_{c,v}(z,r,\theta) = \frac{1}{\sqrt{2\pi}} Z(z) R(r) e^{im\theta} \tag{2.6}$$

The solution for the angular direction is $\frac{1}{\sqrt{2\pi}}\exp(im\theta)$, where m is the angular quantum number taking on values of $0, \pm 1, \pm 2...$ Wavefunction components in the z direction can be calculated using conventional numerical methods – either transfer matrix or finite difference [43]. The transfer matrix approach [43] was used to calculate the wavefunction components in the radial direction, but with Bessel functions being the basis functions. Specifically these are Bessel functions of the first and second kind in regions where the eigen energy is greater than the potential, and modified Bessel functions of the first and second kind when the eigen energy is less than the potential:

$$\begin{aligned} &AJ_v(kr) + BY_v(kr), \text{ if } E_i > V(r) \\ &CI_v(kr) + DK_v(kr), \text{ if } E_i < V(r) \end{aligned} \tag{2.7}$$

The normalization on $Z(z)$ and $R(r)$ was taken as $\int dz Z^2 = 1$ and $\int_0^\infty dr r R^2 = 1$, so that the spatial integration of the total wavefunction over all space is equal to 1. Non-parabolicity effects were not included in this thesis.

2.2 Interaction Hamiltonians

The interactions with photons and phonons are treated in this thesis, and this section gives a first principles derivation to explain the Hamiltonians used.

2.2.1 Electron phonon interaction

For the interaction of electrons with phonons (quantized lattice vibrations), fundamentally they are just coupling between the electronic densities and the displaced lattice potential. This section follows Ref [8]. Starting with the fact that the total Hamiltonian is the sum of the free electron and phonon parts $(H_p + H_e)$ and the interaction part H_{ei},

$$H_{tot} = H_p + H_e + H_{ei} \tag{2.8}$$

H_{ei} is the interaction Hamiltonian between the electrons and lattice ions or atoms. It describes the potential function of the electrons and is given by

$$H_{ei} = \sum_{i,j} V_{latt}(r_i - R_j) \tag{2.9}$$

where r_i are the positions of the electrons, and R_j are the positions of the atoms. After a small displacement of the lattice away from the original position $R_j^{(0)}$, one can Taylor expand the interaction potential

$$V_{latt}(r_i - R_j) = V_{latt}(r_i - R_j^{(0)}) - Q_j \cdot \nabla V_{latt}(r_i - R_j^{(0)}) + \mathcal{O}(Q^2). \tag{2.10}$$

The first term is responsible for the Coulombic interaction, and second term is the well known electron-phonon interaction term, where $Q_j = R_j - R_j^{(0)}$ is the displacement of the atom. The potential V_{latt} can then be decomposed using the Fourier transform,

$$V_{latt}(r) = \frac{1}{N} V_{latt}(q) e^{iq \cdot r} \tag{2.11}$$

where N is the number of atoms or ions. Then taking the spatial derivative yields

$$\nabla V_{latt}(r) = \frac{i}{N} \sum_q q V_{latt}(q) e^{iq \cdot r} \tag{2.12}$$

and substituting back into the first term in Q yields

$$\sum_j Q_j \cdot \nabla V_{latt}(r_i - R_j^{(0)}) = \frac{i}{N} \sum_q \sum_j q V_{latt}(q) e^{iq \cdot r_i} Q_j \cdot e^{-iq \cdot R_j^{(0)}} \tag{2.13}$$

Using the relation between the position operator and the creation and annihilation operators (see Ref. [8])

$$\frac{i}{N} \sum_j Q_j e^{-iq \cdot R_j^{(0)}} = -\sum_q \sqrt{\frac{\hbar}{2m\omega_q N}} \eta (a_q + a_q^\dagger) \tag{2.14}$$

where η is a polarization vector, yields

$$V_{latt}(r) = -\sum_q e^{iq \cdot r} V_{latt}(q) \sqrt{\frac{\hbar}{2m\omega_q N}} \eta (a_q + a_q^\dagger) \tag{2.15}$$

Finally the total interaction Hamiltonian, this is obtained by integrating the potential energy over the spatial charge density $\rho(r)$, which are the energy eigenstates. Finally the electron-phonon Hamiltonian is given by:

$$H_{ep} = \int d^3r \rho(r) V_{latt}(r) \tag{2.16}$$

H_{ep} is related to the original electron-ion Hamiltonian H_{ei} by associating it with the change in the lattice potential. Hence in general, the matrix element or coupling strength depends on two parts. One is from the electron-ion potential and is determined by the specific interaction mechanism. The other part depends on the overlap between the electronic wavefunctions and the wavefunctions of the phonons – this is the so-called form factor [44].

There are different vibrational modes of the lattice. Different phonon branches are shown in Figure 2.1 a) for bulk GaAs. The optical phonons are modes where the atoms oscillate opposite to eachother, and the acoustic modes are oscillating in the same direction (see Figure 2.1 b). For deformation potential coupling to LA phonons, the coupling matrix element is given by

$$M_a^{mm'}(q) = \sqrt{\frac{\hbar\omega_q}{2\rho_M u_s^2 V}} D_a \int d^3r \psi_{ma}^*(r) e^{iq\cdot r} \psi_{m'a}(r) \tag{2.17}$$

where D_a is the deformation of the band a, ω_q is the energy of the LA phonon with wavevector q, ρ_M is the mass density, u_s is the speed of sound, V is the normalization volume, and $\psi(r)$ are the total electronic wavefunctions. The deformation potential is a volume deformation potential, giving the energy change of the potential offset due to the volume change ($\delta E = D\frac{\delta V}{V}$) [47].

The interaction matrix element for LO phonons are given by the Fröhlich electron phonon interaction

$$M_{ab}(q) = i\sqrt{\frac{e^2\hbar\omega_{LO}}{2V\epsilon_0\kappa}} \frac{1}{q} \int d^3r \psi_a^*(r) e^{iq\cdot r} \psi_b(r) \tag{2.18}$$

where ω_{LO} is the LO phonon frequency, $\kappa = \frac{1}{\epsilon_\infty} - \frac{1}{\epsilon_{static}}$. Since the phonon energy around the Γ-point, which is the most revelvant region of wavevectors, does not vary much, it is generally sufficient to approximate using a constant energy $\hbar\omega_{LO}$.

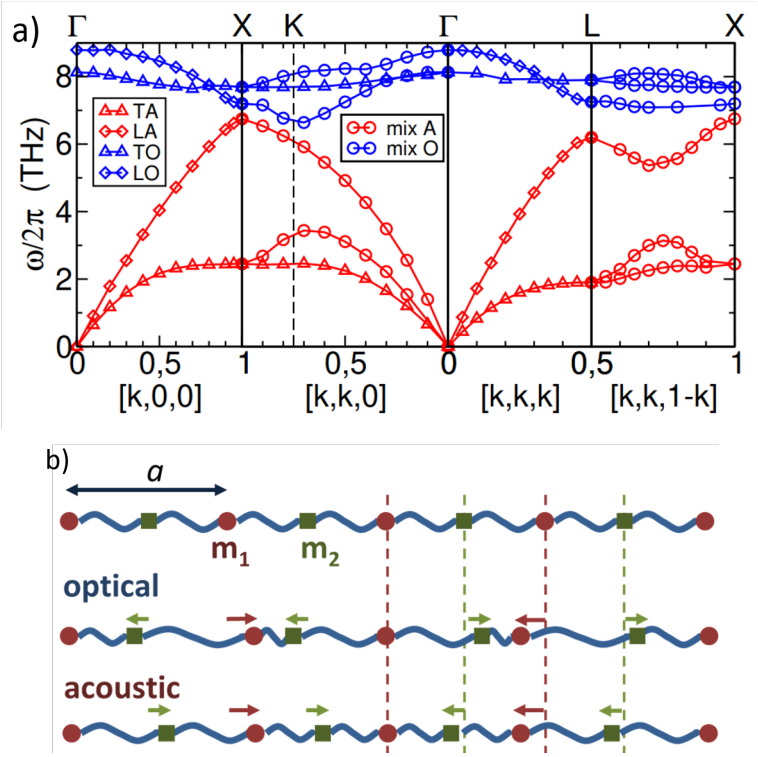

Figure 2.1: a) The phonon dispersion of bulk GaAs. The red lines are the acoustic branches, and blue are the optical branches. The k vector is plotted in units of $2\pi/a$ where $a = 5.653\mathring{A}$ the lattice constant of GaAs, reproduced from [45]. b) Schematic of the optical vs acoustic phonon vibrations, reproduced from [46].

2.2.2 Electron photon interaction

The Hamiltonian of electrons in the prescence of an electromagnetic field is given by

$$H = \frac{(\mathbf{p} - q\mathbf{A})^2}{2m} \tag{2.19}$$

where

$$\mathbf{A}(r) = \sum_{\sigma,q} \sqrt{\frac{\hbar}{2\epsilon_0 \omega_{cav}(q)}} (a_{\sigma,q} u_{\sigma,q}(r) + a^\dagger_{\sigma,q} u^*_{\sigma,q}(r)) \tag{2.20}$$

is the vector potential [48]. Here the $a, a^\dagger$ are the photon creation and annihilation operators, and u are the mode profiles. σ are the polarizations and $\mathbf{q}$ are the wavevectors of the electromagnetic wave. In general one can write $u = \mathbf{e}e^{iq\cdot r}$.

Expanding out the Hamitonian yields the free electron term, a linear interaction term accounting for the coupling between the electron momentum and the electromagnetic field, and a term that is proportional to the vector potential squared.

$$H = \frac{\mathbf{p}^2}{2m} + \frac{e}{m}\mathbf{A}\cdot\mathbf{p} + \frac{e^2}{2m}\mathbf{A}^2 \tag{2.21}$$

If the coupling strength/potential is small, then the squared term can be ignored. Substituting A into the linear electron-light interaction part of the Hamiltonian yields,

$$\begin{aligned} H_{e-l} &= \frac{e}{m}\sum_{\sigma,q}\sqrt{\frac{\hbar}{2\epsilon_0\omega_{cav}(q)}}(a_{\sigma,q}u_{\sigma,q}\cdot p + a^\dagger_{\sigma,q}u^*_{\sigma,q}\cdot p) \\ &= \frac{e}{m}\sum_{\sigma,q}\sqrt{\frac{\hbar}{2\epsilon_0\omega_{cav}(q)}}(a_{\sigma,q}e^{iq\cdot r}\mathbf{e}\cdot p + a^\dagger_{\sigma,q}e^{-iq\cdot r}\mathbf{e}\cdot p) \end{aligned} \tag{2.22}$$

Let's consider the $e^{\pm iq\cdot r}$ terms. If the photon wavelength is much larger than the spatial extent of the QD, then the electrons see a constant electromagentic field, and the approximation that $e^{iq\cdot r}\approx 1$ can be made. This is called the dipole approximation.

The electric field strength is related by

$$E = -i\sqrt{\frac{\hbar\omega}{2\epsilon_0 V}}u(r=0) = -i\sqrt{\frac{\hbar\omega}{2\epsilon_0 V}}\mathbf{e} \tag{2.23}$$

and using the relation between the momentum and the position operator that $z_{ba} = \frac{\hbar}{iE_{ba}m}p_{ba}$, the familiar dipole interaction Hamiltonian is obtained, given by

$$\begin{aligned} H &= -ez_{ba}\cdot E_0 \\ &= \mu E_0 \end{aligned} \tag{2.24}$$

2.3 Basic quantum transport formalisms

In this section basic quantum transport concepts are introduced. References include [49, 8, 50]. The Dyson's equation is presented, which is at the heart of the cumulant expansion (linked cluster) approach used in the interband QD dyanmics in Chapter 3. The concept of the density matrix and its time evolution and different pictures of quantum mechanics, as well as common approximations are explained. These are the background knowledge for the scattering transport for the QDCL section (Chapter 4). Lastly, relations to the more widely known concepts such as rate equations are made for some intuitive understandings.

2.3.1 Time Evolution

Given a state $|\psi(t)\rangle$ at initial time t_0, its time evolution follows the time-dependent Schrödinger equation,

$$i\hbar\frac{d}{dt}|\psi(t)\rangle = H|\psi(t)\rangle \tag{2.25}$$

This has the solution $U(t,t_0)$

$$|\psi(t)\rangle = U(t,t_0)|\psi(t_0)\rangle \tag{2.26}$$

where $U(t,t_0)$ is the time evolution operator. If the Hamiltonian of the system H is independent of time, then the solution is trivial and the unitary evolution operator $U(t,t_0) = \exp(\frac{-iH(t-t_0)}{\hbar})$. For the most general case, if the Hamiltonian is time-dependent and do not commute with itself at different times, then

$$U(t,t_0) = \mathcal{T}\big(e^{\frac{-i}{\hbar}\int_{t_0}^{t} dt' H(t')}\big) \tag{2.27}$$

Here $\mathcal{T}$ is the time ordering operator which orders operators with increasing time from right to left. This time operator is an abbreviation for the following series:

$$= 1 + \sum_{n=1}^{\infty}\Big(\frac{-i}{n}\Big)^n \int_{t_0}^{t} dt_1 \int_{t_0}^{t_1} dt_2 ... \int_{t_0}^{t_{n-1}} dt_n H(t_1)H(t_2)...H(t_n) \tag{2.28}$$

this is also known as the Dyson series.

2.3.2 Density Matrix

To keep track of the states of the system, the density matrix formalism is used. Given a basis set

$$|\psi(t)\rangle = \sum_n c_n(t)|n\rangle \tag{2.29}$$

The density operator is defined by

$$\rho \equiv |\psi(t)\rangle\langle\psi(t)| = \sum_{nm} c_n(t)c_m^*(t)|n\rangle\langle m| \tag{2.30}$$

hence the density matrix elements are $\rho_{nm}(t) = c_n(t)c_m^*(t)$. The diagonal elements are the populations while the off-diagonals are the coherences. Its time evolution is given by

$$\rho(t) = U(t,t_0)\rho(t_0)U^\dagger(t,t_0) \tag{2.31}$$

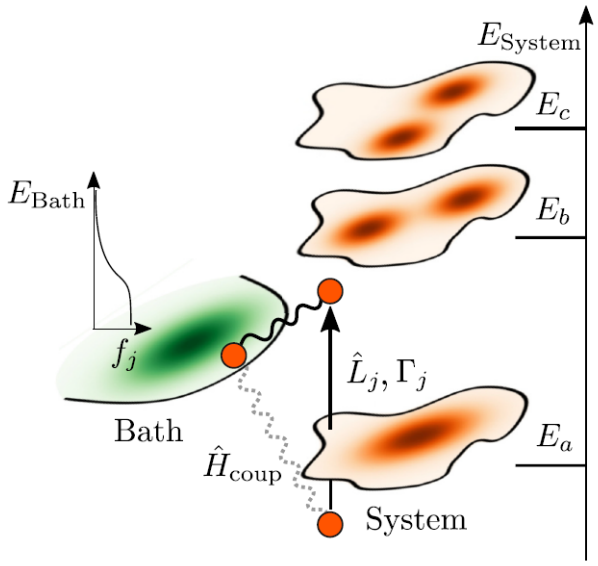

Figure 2.2: The paradigm problem of a few level system coupled to a heat bath. Reproduced from Ref. [51]

The density matrix has the properties that $Tr(\rho(t)) = 1$. The density matrix has is an observable and hence it is Hermitian. It is also positive semi-definite (meaning that it has positive eigen-values).

There are three different pictures of quantum mechanics; the Schrodinger picture where the states evolve in time but operators do not, the Heisenberg picture where only the operators evolve in time, and the interaction picture where both states and operators evolve in time. From the Schrödinger's equation, the Liouville von-Neumann equation can be derived (which is just the equations of motion in the Schrodinger picture)

$$\frac{d}{dt}\rho(t) = -\frac{i}{\hbar}[H, \rho(t)] \tag{2.32}$$

In comparison, the Heisenberg's equation of motion says that

$$\frac{d}{dt}\rho(t) = \frac{i}{\hbar}[H, \rho(t)] \tag{2.33}$$

If one has enough resources to model the entire many body system, then the use of either of these approaches do not have a difference in the final observables. However typically one cannot model the entire system and this is where approximations come in. For example, one

of the common steps is to assume the density matrix can be factorized as a tensor product of the system and reservoir part, which is valid if there are no correlations between those subsystems.

$$\rho = \rho_S \otimes \rho_R \tag{2.34}$$

One can also assume that the reservoir remains unchanged for all times during which the system evolves, because the reservoir is so large that a tiny perturbation from the system does not make a noticeable change in the bath, and hence

$$\rho(t) = \rho_S(t) \otimes \rho_R(t_0) \tag{2.35}$$

This is the so-called Born approximation. Now if there are correlations between those subsystems, typically the Heisenberg picture is used to arrive at correlation expansion based approaches. This is used in for example in systems where there are strong correlations between a few electron and photon states, and one needs to keep track of the correlations between those.

In the interaction approach one starts with the Liouville-von Neumann equation, then transform it to the interaction picture, yielding

$$\frac{d\rho_I(t)}{dt} = \frac{-i}{\hbar}[H_I(t), \rho_I(t)] \tag{2.36}$$

Integrating this yields

$$\rho_I(t) = \rho_I(t_0) - i\int_{t_0}^{t} dt'[H_I(t'), \rho_I(t)] \tag{2.37}$$

Substitution back into the derivative and taking the trace over the bath yields the equation in integro-differential form

$$\frac{d\rho_S(t)}{dt} = \frac{-1}{\hbar^2}\int_0^t dt' Tr_R[H_I(t), [H_I(t'), \rho(t') \otimes R_0]]. \tag{2.38}$$

Subsequently, one can go to higher orders in the memory kernal, or one can make Markov approximations. For example if one makes the approximation that $t' = t$, then the time evolution of ρ only depends on its current state and not its past states – some of the memory features are elminated. This is the first Markov approximation. A second Markov approximation can be made if the upper limit of the integral is extended to infinity. Equation 2.38 is the starting point for many different forms of the time evolution equations, including Redfield/time convolutionless master equations, as well as Lindblad equations.

2.3.3 Intuitive Associations to Semiclassical Concepts

Although there are many different quantum kinetic approaches, they should all recover the semiclassical Boltzmann (rate) equations. The rate equations state that the change of population in time is equal to that incoming minus that outgoing from the said state.

$$\frac{dn_i}{dt} = -\sum_j \frac{n_i}{\tau_{i\to j}} + \sum_j \frac{n_j}{\tau_{j\to i}} \tag{2.39}$$

In this equation the transport times are given by the famous Fermi's Golden rule, which says that

$$\Gamma_{i\to f} = \sum_f \frac{2\pi}{\hbar} |\langle f| H_{int} |i\rangle|^2 g_f(E)\delta(E_f - E_i \pm \hbar\omega) \tag{2.40}$$

where $g_f(E_i)$ is the density of final states for which the energy conservation is satisfied, and H_{int} is the interaction matrix element. This is also known as a T_1 time in the literature. T_1 times describe a population change, and is associated with a loss of energy. There are also T_2 times, which describe the dephasing, i.e. the loss of coherence. It is how the off-diagonal elements of the density matrix decay. This is usually implemented as

$$\frac{1}{T_2} = \frac{1}{\tau^*} + \frac{1}{2\tau_{\text{lifetime}}} \tag{2.41}$$

where τ^* is a pure dephasing time, and τ_{lifetime} are the level lifetimes which include the total loss of populations in the said state. The pure dephasing time describes a loss of coherence without a net change in the populations.

For strong interactions, Fermi's Golden Rule (FGR) and rate equations approaches are not enough. This is because FGR describes irreversible dynamics. Whether or not the interaction is considered strong is determined by comparison to the other decoherence channels in the system. For example, consider a two level system in the prescence of phonons, as illustrated in Figure 2.3. The electron starts in the excited state. Then through interaction with the phonon it transitions down to the ground state, emitting a phonon. Now since the phonon is still in the system, it can be reabsorbed, promoting the ground state electron to the excited state again. This back and forth reabsorption and emission creates the quasi-particle called a polaron. On the other hand, if the optical phonon has fast decay to phonons of lower energy (e.g. acoustic phonons) then it cannot be absorbed, and this is the weak interaction regime.

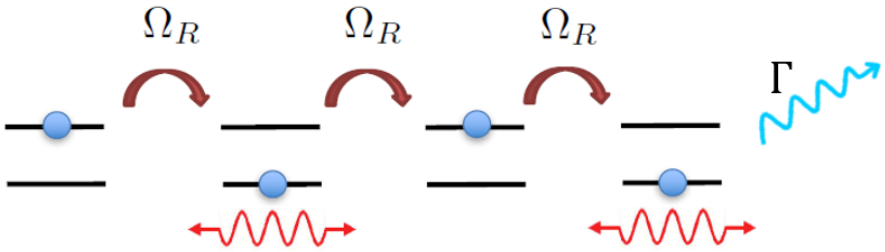

Figure 2.3: Illustration of transitions in the strong coupling regime. The black lines denote the excited and ground state of the electron, Ω_R is the interaction strength to the reservoir, Γ is the decay rate of the reservoir particle, and the red wavepackets are the reservoir particles. Modified from Ref [52].

Chapter 3

Interband Dynamics

This chapter presents work on the spectra of interband optical transitions from QDs in semiconductor nanowires, broadened due to interactions with phonons. The theory follows the Independent Boson model with additional quadratic broadening. It is now well known that the diagonal coupling results in broad phonon sidebands in the emission spectra of QDs. However, it was discovered early on that the diagonal coupling has residual coherence that does not decay out. This then leads to an infinitely sharp ZPL which is not physically correct. Physical mechanisms that lead to the decay of the ZPL include spontaneous emission, non-radiative recombination, anharmonicity, virtual interactions etc. The broadening of the ZPL is included through the virtual interactions. Essentially, it accounts for the decoherence due to back and forth emission and re-absorption of phonons by the QD. This interaction is derived by performing a Schrieffer and Wolff transformation on the non-diagonal part of the interaction, which results in a coupling that is quadratic in the phonon displacement operators. This Hamiltonian can either be approximated or solved numercially exact by using a Fredholm integral eigenvalue approach. The theory is compared to experimental data, and structural and material variations of the QD are investigated.

3.1 Time evolution of the microscopic coherence

Let's follow the dynamics of the QD coherence as it's coupled to the phonon environment. The polarization for an excited QD exciton after a delta pulse excitation is given by

$$\begin{aligned} P(t) &= i\langle\sigma^+(t)\sigma^-(0)\rangle \\ &= i\langle e^{iHt}\sigma^+(0)e^{-iHt}\sigma^-(0)\rangle, \end{aligned} \tag{3.1}$$

Where H is the model Hamiltonian $H = H_0 + V_{e-ph}$ consisting of the free evolution and interaction parts

$$\begin{aligned} H_0 &= H_e + H_{ph} = \sum_i \hbar\omega_i \left|i\right\rangle \left\langle i\right| + \sum_q \hbar\omega_q b_q^\dagger b_q \\ V_{e-ph} &= \sum_{nm}\sum_q M_{nm} \left|n\right\rangle \left\langle m\right| (b_q + b_{-q}^\dagger) = H_d + H_{nd} \end{aligned} \tag{3.2}$$

V_{e-ph} is the electron phonon interaction term, and the sum over n and m is for all electrons in valence band and conduction band. It contains both diagonal (H_d) and non-diagonal (H_{nd}) interactions. From an optical excitation, an electron from the valence band is excited to the conduction band. Due to the optical transition, the surrounding lattice ions undergo deformations to a new equilibrium position, resulting in the electron phonon interactions.

Now restricting ourselves to just the one exciton $H_e = \hbar\omega_x \left|1\right\rangle \left\langle 1\right|$, and substituting the total Hamiltonian into the time evolution of the coherence term yields

$$\begin{aligned} &= i\langle\sigma^+(0)\sigma^-(0)\rangle\langle e^{i(H_{ph}+H_e+V_{e-ph})t}e^{-iH_{ph}t}\rangle \\ &= i\rho_{ee}(0)e^{i(\omega_x+\Delta_p)t}\langle e^{i(H_{ph}+V_{e-ph})t}e^{-iH_{ph}t}\rangle \\ &= ie^{i(\omega_x+\Delta_p)t}\left\langle \mathcal{T}\exp(-\frac{i}{\hbar}\int_0^t d\tau V_{e-ph}(\tau))\right\rangle \end{aligned} \tag{3.3}$$

Where Δ_p is an energy (polaron) shift, and $\rho_{ee}(0) = 1$. The assumption of just one exciton (electron-hole) in our system is valid at low temperatures and low excitation powers, however virtual or intermediate states are included in the K_Q interaction.

The next sections will present the evaluation of this time ordered integral – first for diagonal interactions and then the non-diagonal interactions.

3.2 Independent Boson Model

The Independent Boson Model (IBM) is the exact solution to the e-phonon diagonal coupling, after a delta-pulse excitation. In this case only the loss of the microscopic coherence is analyzed and not the change of the occupations in the system.

First, to define the ground state as being non-interacting, the displaced phonon operators (Weyl operators) are used. This is also called performing a Huang Rhys transformation $b_q \rightarrow b_q - \frac{M_{gg}}{\hbar\omega_q}$, and yields

$$H' = \sum_i \tilde{E}_i c_i^\dagger c_i + H_{ph} + \sum_i \sum_q \tilde{M}_i \left|i\right\rangle \left\langle i\right| (b_q + b_{-q}^\dagger) \tag{3.4}$$

where $\tilde{M}_{ii} = M_{ii} - M_{gg}$, and M_{gg} is the interaction matrix element of the ground states. Here the ground state is defined as the s state in the valence band. The electronic energies are renormalized by $2\sum_q (M_{ii}^q - M_{gg}^q)\frac{M_{gg}^q}{\hbar\omega_g}$ due to this transformation. [53]

Next this is plugged into equation 3.3 and evaluate the time-ordered exponential operator. This can be written in the following form:

$$\sum_{n=0}^{\infty} (-i)^n \frac{\lambda^n}{n!} \int_0^t dt_1 \int_0^t dt_2 ... \int_0^t dt_n \langle \mathcal{T} A(t_1)...A(t_n)\rangle \tag{3.5}$$

where $A(t) = be^{-i\omega t} + b^\dagger e^{i\omega t}$, and $\lambda = \tilde{M}_{ii}$ is the interaction strength [8]. The Wick's theorem is then used to find that the pairs of A operators $\langle \mathcal{T} A(t_1)A(t_2)\rangle$ evaluate to the phonon Green's function $iD_q(|t_1 - t_2|) = [(N_q + 1)e^{-i\omega_q|t_1-t_2|} + N_q e^{i\omega_q|t_1-t_2|}]$, where $N_q = 1/(e^{\hbar\omega/kT} - 1)$ the thermal Bose distribution. Analytically carrying out the double time integral over the phonon Green's function

$$\int_0^t dt_1 \int_0^t dt_2 [(N_q + 1)e^{-i\omega_q|t_1-t_2|} + N_q e^{i\omega_q|t_1-t_2|}] \tag{3.6}$$

defines a function

$$\Phi(t) = \frac{2}{\omega_q^2}[(N_q + 1)(1 - e^{-i\omega_q t}) + N_q(1 - e^{i\omega_q t}) - i\omega_q t]. \tag{3.7}$$

Now for each pair of phonons, or in other words $n = 2m$ number of phonons, there are a possible $\frac{(2m)!}{2^m m!}$ combinations of them to pair up, and this factor gets multiplied infront. Putting everything together into equation 3.5,

$$\sum_m \frac{\lambda^{2m}}{m!} \left[\frac{\Phi(t)}{2}\right]^m \tag{3.8}$$

which is just the Taylor series expansion for an exponential function. In the literature this is known as the linear cumulant term, written as

$$\exp\Big[-\frac{\lambda^2}{2}\Phi(t)\Big] = \exp(K_L(t)) \tag{3.9}$$

where

$$\begin{aligned} K_L(t) &= \frac{-i}{2\hbar}\int_0^t dt_1 \int_0^t dt_2 \sum_q |M_q|^2 D_q(t_1 - t_2) \\ &= \frac{-1}{\hbar^2}\sum_q |M_q|^2 \frac{1}{\omega_q^2}[(N_q+1)(1-e^{-i\omega_q t}) + N_q(1-e^{i\omega_q t}) - i\omega_q t]. \end{aligned} \tag{3.10}$$

This equation is valid for both LA and LO phonons. From this it is clear that the cumulant is over an infinite sum and this solution is exact.

The next step is substitute the specific interaction potentials, and carry out the summation over q for numerical evaluation. For the deformation potential coupling to LA phonons, the coupling matrix elements is given by

$$M_{qa}^{mm'} = \sqrt{\frac{\hbar\omega_q}{2\rho_M u_s^2 V}} D_a \int d^3r \psi_{ma}^*(r) e^{iq\cdot r} \psi_{m'a}(r) \tag{3.11}$$

where D_a is the deformation potential for the conduction or valence band ($a = c$ for electrons or v for holes), ρ_M is the mass density, u_s is the longitudinal speed of sound, and V is a normalization volume. The subscript c or v on the matrix elements correspond to either the electron or hole wavefunctions. LO phonons were not included in the diagonal interaction in this thesis, since this should be small contribution.

The math for the LA phonon interaction is treated as follows:

$$\begin{aligned} \sum_q |M_q|^2 &= \sum_q |M_{qe} - M_{qh}|^2 \\ &= \sum_q \frac{\hbar\omega_q}{2\rho u_s^2 V} |D_e \int d^3r \psi_{1e}^* e^{i\vec{q}\cdot\vec{r}} \psi_{1e} - D_v \int d^3r \psi_{1h}^* e^{i\vec{q}\cdot\vec{r}} \psi_{1h}|^2 \end{aligned} \tag{3.12}$$

Converting the sum over q to an integral $\sum_q \to \int d^3q \frac{V}{(2\pi)^3}$ and using cylindrical coordinates yields,

$$\begin{aligned} &= \int d^3q \frac{V}{(2\pi)^3} \frac{\hbar\omega_q}{2\rho u_s^2 V} |D_e \int d^3r \psi_{1e}^* e^{i\vec{q}\cdot\vec{r}} \psi_{1e} - D_v \int d^3r \psi_{1h}^* e^{i\vec{q}\cdot\vec{r}} \psi_{1h}|^2 \\ &= \frac{\hbar}{(2\pi)^2 2\rho u_s} \int_0^\infty dq_r q_r \int_{-\infty}^\infty dq_z q |D_e \int d^3r \psi_{1e}^* e^{i\vec{q}\cdot\vec{r}} \psi_{1e} - D_v \int d^3r \psi_{1h}^* e^{i\vec{q}\cdot\vec{r}} \psi_{1h}|^2 \end{aligned} \tag{3.13}$$

where $q = \sqrt{q_r^2 + q_z^2}$ the magnitude of the total wavevector of the LA phonons. Evaluation of the form factor of the type $\int d^3r \psi_1^* e^{i\vec{q}\cdot\vec{r}} \psi_2$ proceeds by expanding plane wave in cylindrical coordinates [34], and is explained in Appendix 3.7. Converting the integration over q_r to E leads to the final equation implemented for K_L:

K_L for LA phonons

$$K_L(t) = \frac{-1}{8\pi^2\hbar^2 u_s^4 \rho_M} \int_0^\infty dE \int_{-E/\hbar u_s}^{E/\hbar u_s} dq_z |D_c \int d^3r \psi_{1e} e^{i\vec{q}\cdot\vec{r}} \psi_{1e} - D_v \int d^3r \psi_{1h} e^{i\vec{q}\cdot\vec{r}} \psi_{1h}|^2 \times [(N_q + 1)(1 - e^{-i\omega_q t}) + N_q(1 - e^{i\omega_q t}) - i\omega_q t]. \tag{3.14}$$

3.3 Quadratic coupling

This section presents the treatment of the non-diagonal interactions, which mainly follows Refs [8, 54].

First a Schrieffer and Wolff transformation $H' = e^S H e^{-S}$ is performed on the non-diagonal part of the interaction Hamiltonian. The purpose of this is to write the non-diagonal interaction in a diagonal form so that the cumulant expansion can be evaluated. The trick is to choose the transformation operator S such that $[S, H_0] = -H_{nd}$, and is given by [54]

$$S = \sum_{n,m,q} |n\rangle \langle m| M_{nm} \left(\frac{b_q}{E_n - E_m - \omega_q} + \frac{b_{-q}^\dagger}{E_n - E_m + \omega_q} \right), \tag{3.15}$$

where $E_{n,m}$ are the electronic eigen energies and ω_q is the LA or LO phonon energy. In this way, $H' = e^S H e^{-S} \approx H_0 + \frac{1}{2}[S, H_{nd}]$, which, upon adding in the diagonal interaction results in the total model Hamiltonian,

$$\begin{aligned} H' &= \sum_i \tilde{E}_i c_e^\dagger c_e + \sum_q \hbar\omega_q b_q^\dagger b_q + \sum_{m,qp} \frac{M_{nm}(q) M_{mn}(p)}{\Delta_{nm}} |n\rangle \langle n| (b_q + b_q^\dagger)(b_p + b_p^\dagger) \\ &+ \sum_q M(q) |e\rangle \langle e| (b_q + b_{-q}^\dagger) \\ &= H_e + H_{ph} + V_L + V_Q. \end{aligned} \tag{3.16}$$

From this one sees that there are terms that are linear (V_L) and quadratic (V_Q) in phonon displacement operators. Here $1/\Delta_{nm} = (E_n - E_m)/((E_n - E_m)^2 - (\hbar\omega_{LO})^2)$. In addition, $\tilde{E}_i$ is now renormalized due to the quadratic term, $\sum_{m,q} \frac{M_{im}M_{mi}\omega_q}{(E_i - E_m)^2 - \omega_q^2}$.

Again, the ground state may be re-defined as being non-interacting, by performing the Huang Rhys transformation $b_q \to b_q - \frac{M_{gg}}{\hbar\omega_q}$, to obtain

$$\begin{aligned} H' = &\sum_i \tilde{E}_i c_i^\dagger c_i + H_{ph} + \sum_n \sum_q \tilde{M}_n \left|n\right\rangle \left\langle n\right| (b_q + b_{-q}^\dagger) \\ &+ \sum_{q,q'} \sum_{nm,n\neq m} \frac{M_{nm}M_{mn}}{\Delta_{nm}} \left|n\right\rangle \left\langle n\right| (b_q + b_{-q}^\dagger)(b_{q'} + b_{-q'}^\dagger) \end{aligned} \tag{3.17}$$

where $\tilde{M}_{nn} = M_{nn} - M_{gg}$, and the electronic energies are renormalized again by $2\sum_q (M_{ii}^q - M_{gg}^q)\frac{M_{gg}^q}{\hbar\omega_g}$. To summarize, the form of the equations which are valid for both the LO and LA phonon interactions are,

$$\begin{aligned} V_L &= \sum_q M_q (b_q + b_{-q}^\dagger), \\ M_q &= M_{qe}^{11} - M_{qh}^{11}, \\ V_Q &= \sum_{q,q'} Q_{q,q'} (b_q + b_{-q}^\dagger)(b_{q'} + b_{-q'}^\dagger), \\ Q_{q,q'} &= \sum_{a=c,v} \sum_{m\neq 1} \frac{(M_{qa}^{1m} M_{q'a}^{m1})(E_m^a - E_1^a)}{(E_m^a - E_1^a)^2 - w_q^2}, \end{aligned} \tag{3.18}$$

Note that the ω_q in $Q_{q,q'}$ was ignored in [11] for LA phonons, which is valid if the energy spacings are relatively large.

Now let's proceed to see how the quadratic interaction affects the time evolution of the polarization. The quadratic interaction part of the time ordered exponential (K_Q) is given by

$$K_Q(t) = \sum_{n=1}^{\infty} \left(\frac{-i}{\hbar}\right)^n \frac{1}{n!} \int_0^t dt_1 \int_0^t dt_2 ... \int_0^t dt_n \Big\langle \mathcal{T} V_Q(t_1) V_Q(t_2) ... V_Q(t_n) \Big\rangle_{conn} \tag{3.19}$$

which is equivalent to

$$= \sum_{n=1}^{\infty} \frac{\lambda'^n}{2n} \int_0^t dt_1 \int_0^t dt_2 ... \int_0^t dt_n D(t_1 - t_2) D(t_2 - t_3) ... D(t_n - t_1) \tag{3.20}$$

To carry out this infinite series of integrals, it is recognized that this is in the form of a Fredholm eigenvalue problem, given by [55]

$$\int_0^t d\tau' D(\tau - \tau') u_j(\tau'; t) = \Lambda_j(t) u_j(\tau; t). \tag{3.21}$$

Rewriting this as a matrix eigenvalue problem,

$$\begin{bmatrix} D(t_0,t_0) & D(t_0,t_1) & D(t_0,t_2)... \\ D(t_1,t_0) & D(t_1,t_1) & D(t_1,t_2)... \\ ... & & \end{bmatrix} \begin{bmatrix} u_j(t_0) \\ u_j(t_1) \\ ... \end{bmatrix} dt = \Lambda_j \begin{bmatrix} u_j(t_0) \\ u_j(t_1) \\ ... \end{bmatrix}. \tag{3.22}$$

The eigenvalues of the matrix in magenta is summed to give the value of the series of integrals over D. This gives

$$K_Q(t) = \sum_j \sum_{n=1}^{\infty} \frac{\lambda'^n}{2n} \Lambda_j^n(t) \tag{3.23}$$

where $\lambda' = 2\lambda$ and Λ are the eigen values from the Fredholm problem. Using the identity that $-\frac{1}{2}\ln(1-x) = \sum_n \frac{x^n}{2n}$, one can relate to eqn 7 of Ref [55]:

K_Q for LO phonons

$$K_Q(t) = -\sum_{j,v} \frac{1}{2} \ln(1 - i\lambda'_v \Lambda_j) \tag{3.24}$$

where λ'_v are the eigenvalues of the interaction matrix. To summarize, the quadratic interaction is

$$V_Q = \sum_m |n\rangle \langle n| M_{nm} M_{mn} \frac{(E_n - E_m)}{(E_n - E_m)^2 - \omega_0^2} (b_q + b^\dagger_{-q})(b_p + b^\dagger_{-p}) \tag{3.25}$$

and the Kernel for which the Fredholm problem is solved for is

$$D(t_1, t_2) = \left(\frac{-i}{\hbar}\right) \left[(N_q + 1) e^{-i\omega_q |t_1 - t_2|} + N_q e^{i\omega_q |t_1 - t_2|}\right] e^{-\gamma |t_1 - t_2|} \tag{3.26}$$

where γ is the decay rate of the LO phonons [56]. The coupling strength is

$$\lambda' = \frac{1}{\Delta} \frac{e^2 \hbar \omega_q}{4\pi^2 \kappa} \int_0^\infty dq_r q_r \int_{-\infty}^{\infty} dq_z \frac{F_{1jj1}(q_r, q_z)}{q^2} \tag{3.27}$$

and the eigenvalues of this is used.

For LA phonons, approximation of its quadratic interaction at the second order in the summation is sufficient, while for LO phonons the full series of time integrals needs to be solved via the Fredholm integral eigenvalue equation. This is most likely due to the presence of a range of the phonon energies for LA phonons, thus causing more interference effects.

For LA phonons, the function K_Q is given by

$$\begin{aligned} K_Q^{n=2}(t) &= \frac{1}{4}\int_0^t dt_1 \int_0^t dt_2 D_Q(t_1 - t_2) D_Q(t_2 - t_1) \\ &= \frac{-1}{\triangle^2 \hbar^2} \sum_{q_1} |M_{q1}^{12}|^2 \sum_{q_2} |M_{q2}^{12}|^2 \tilde{D}(q_1, q_2, t) \end{aligned} \tag{3.28}$$

where

$$D_Q(t) = \frac{-2}{\triangle} \sum_q |M_q^{12}|^2 \big(\frac{-i}{\hbar}\big)[(N_q + 1)e^{-i\omega_q|t|} + N_q e^{i\omega_q|t|}] \tag{3.29}$$

and

$$\begin{aligned} \tilde{D}(q_1, q_2, t) = \int_0^t dt_1 \int_0^t dt_2 &[(N_{q_1} + 1)e^{-i\omega_{q_1}|t_1 - t_2|} + N_{q_1} e^{i\omega_{q1}|t_1 - t_2|}] \\ &\times [(N_{q_2} + 1)e^{-i\omega_{q_2}|t_2 - t_1|} + N_{q_2} e^{i\omega_{q2}|t_2 - t_1|}] \end{aligned} \tag{3.30}$$

The first term $n = 1$ does not contribute [14]. For the evaluation of the matrix elements

$$|M_q^{12}|^2 = \frac{\hbar q}{2\rho_M u_s V} D_a^2 | \int d^3 r \psi_{1a}^* e^{i\vec{q}\cdot\vec{r}} \psi_{2a}|^2 \tag{3.31}$$

The integral evaluates to (see Appendix 3.7 for details)

$$\begin{aligned} |\int d^3 r \psi_{1a}^* e^{i\vec{q}\cdot\vec{r}} \psi_{2a}|^2 &= |F_z^{12}(q_z)|^2 |F_r^{12}(q_r)|^2 \\ |F_z^{12}(q_z)|^2 &= |\int_{-\infty}^{+\infty} dz e^{iq_z z} Z_1 Z_2|^2 \\ |F_r^{12}(q_r)|^2 &= |\int_0^{\infty} dr r R_1 R_2 J_n(q_r r)|^2 \end{aligned} \tag{3.32}$$

where n is the change in angular momentum. Substitution of these form factors and turning the sums into integrals yield

$$K_Q^{n=2}(t) = \frac{-\hbar^2 D_a^4}{\triangle^2 \hbar^2 (2\pi)^6 (2\rho_M u_s)^2} \int d^3q_1 q_1 |F_r^{12}(q_{r1})|^2 |F_z^{12}(q_{z1})|^2 \\ \times \int d^3q_2 q_2 |F_r^{12}(q_{r2})|^2 |F_z^{12}(q_{z2})|^2 \times \tilde{D}(q_1, q_2, t) \tag{3.33}$$

After converting to cylindrical coordinates, and changing integration variables from q_r to E,

$$K_Q^{n=2}(t) = \frac{-D_a^4}{\triangle^2 (2\pi)^4 (2\rho_M u_s)^2} \int_0^\infty dE_1 \int_{-E/\hbar u_s}^{E/\hbar u_s} dq_{z1} \frac{E_1^2}{(\hbar u_s)^3} |F_z^{12}(q_{z1})|^2 |F_r^{12}(q_{r1})|^2 \\ \times \int_0^\infty dE_2 \int_{-E/\hbar u_s}^{E/\hbar u_s} dq_{z2} \frac{E_2^2}{(\hbar u_s)^3} |F_z^{12}(q_{z2})|^2 |F_r^{12}(q_{r2})|^2 \times \tilde{D}(q_1, q_2, t). \tag{3.34}$$

Now if ignoring contributions from terms describing emission of two phonons or absorption of two phonons, ignoring imaginary terms, and taking the long time limit, $\tilde{D}(q_1, q_2, t)$ integrates to [14]

$$\tilde{D}(q_1, q_2, t) \simeq 2(2N_{q_1} N_{q_2} + N_{q_1} + N_{q_2}) \pi \hbar \delta(E_1 - E_2) t. \tag{3.35}$$

The energy conserving delta is illustrative of the physical mechanism behind this K_Q term - the simultaneous emission and absorption of phonons of the same energy results in a change in the phase of the dipole and hence broadening of the spectrum [57].

The final equation for K_Q of LA phonons is

K_Q for LA phonons

$$K_Q^{n=2}(t) = \frac{-D_a^4}{\triangle^2 2^4 \pi^3 \rho_M^2 u_s^8 \hbar^5} \int_0^\infty dE \int_{-E/\hbar u_s}^{E/\hbar u_s} dq_{z1} \int_{-E/\hbar u_s}^{E/\hbar u_s} dq_{z2} E^4 |F_z^{12}(q_{z1})|^2 |F_r^{12}(q_{r1})|^2 \\ |F_z^{12}(q_{z2})|^2 |F_r^{12}(q_{r2})|^2 N_q (N_q + 1) t \\ = -\Gamma_{3D} t \tag{3.36}$$

This is nothing but an exponential decay of the coherence, resulting in a Lorentzian broadening of the ZPL.

3.4 Simulation Flow

Constructing everything together, the polarization evolves as

$$P(t) = \exp(-i\omega_0 t + K_L^{LA}(t) + K_Q^{LA}(t) + K_Q^{LO}(t)) \tag{3.37}$$

There is also a mixed term K_M, which comes from mixing of V_L and V_Q [14]; for our calculations, K_M is neglected, which is valid for parity symmetric wavefunctions and environments [14]. It has been ignored in other related works as well [55, 14].

The basic simulation flow is shown in Figure 3.1. First the simulation parameters and conditions are input. Then the band structure is calculated. Obviously, if the wavefunctions appear to have the expected shape (e.g. not diverging) then it is probable that they are calculated correctly. One way to establish some confidence in the wavefunctions calculated is to compare to the experimentally obtained energy spacings. Once satisfied with the calculated wavefunctions, these can then be used to calculate for the K_Q and K_L of the LA and LO phonons. During these steps one should make sure that a large enough range of the phonon energy or wavevector is used in calculating the formfactors. The polarization should also be calculated to long enough of a time such that it has decayed enough to take a Fourier transform. Finally, the emission spectrum can be calculated using the Fourier transform of the polarization of time. The spectra are also normalized such that their maximum value is 1.

3.5 Results

3.5.1 Structural Variations

In this subsection, the numerical results in which the radius and height of QDs in wells are varied are shown. First the effect of only the LA phonons is shown , then with the LO phonons as well. This also serves as somewhat of a fitting procedure to the experimental data for the structure shown in Fig. 3.2, which will be analyzed in section 3.5.2. Figure 3.3 shows the calculated wavefunctions for this type of geometry. The factorization of the wavefunctions leads to the quantum numbers n_z in the z direction, and (m,n_r) for the radial direction. These are labeled in Fig. 3.3; m is the angular momentum quantum number, and n_r denotes the n_r^{th} eigenenergy level associated with m. The total eigenenergy is given by $E = E_{n_z} + E_{m,n_r}$.

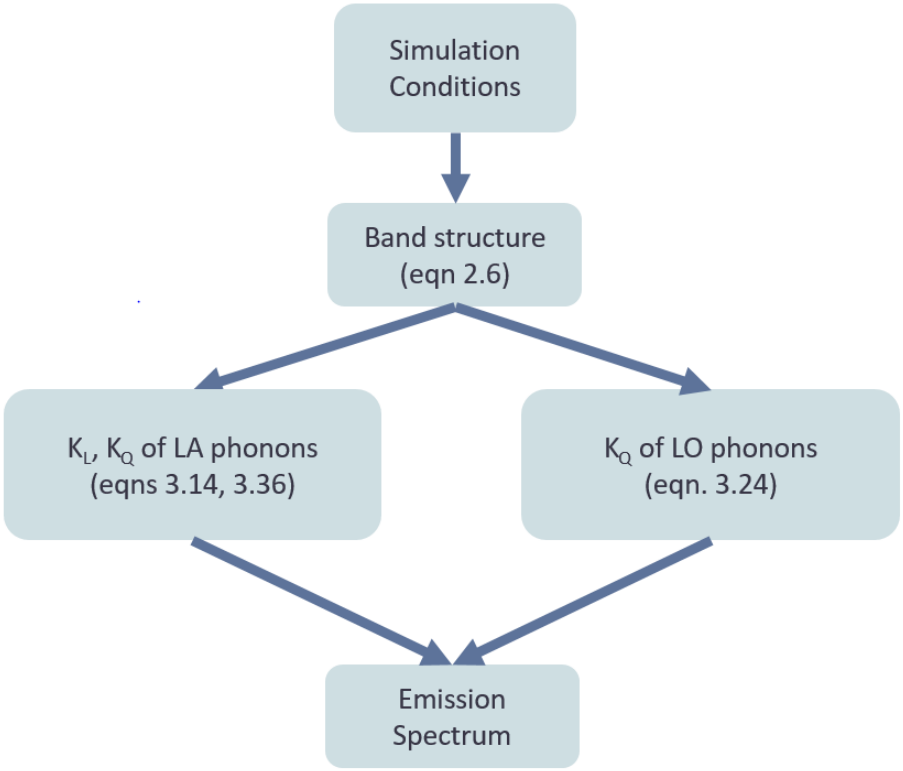

Figure 3.1: The basic simulation flow is illustrated.

The structural variations including only LA phonons are shown in Figure 3.4. The radius and height (h_{dot} in Figure 3.2) of the QD are varied. Only the state closest in energy to the ground state in the conduction and valence bands were taken into account in the calculations in order to highlight the main trends. Equations 3.14 and 3.36 are the main equations used to calculate the spectrum. Comparing the spectra of 4-nm (Figure 3.4 a) and 9.5-nm radius (Figure 3.4 c), smaller QDs can be coupled to phonons with larger energies and hence result in the wider sidebands. In the case of 4-nm radius, the first excited state in the valence band is the n_z=2, m=0 state for all the heights shown. As shown in Fig. 3.4 b), in the height range of 4-7 nm, the first excited state in the conduction band is the p state, and in the height range of 8-10 nm height, the first excited state is the n_z=2,m=0 state. The decrease in energy spacing in the z direction with increasing QD height resulted in a net increase in the ZPL broadening and hence effectively higher height of pedestals as well. In the case of 9.5-nm radius [see Fig. 3.4(c) and (d)], the first

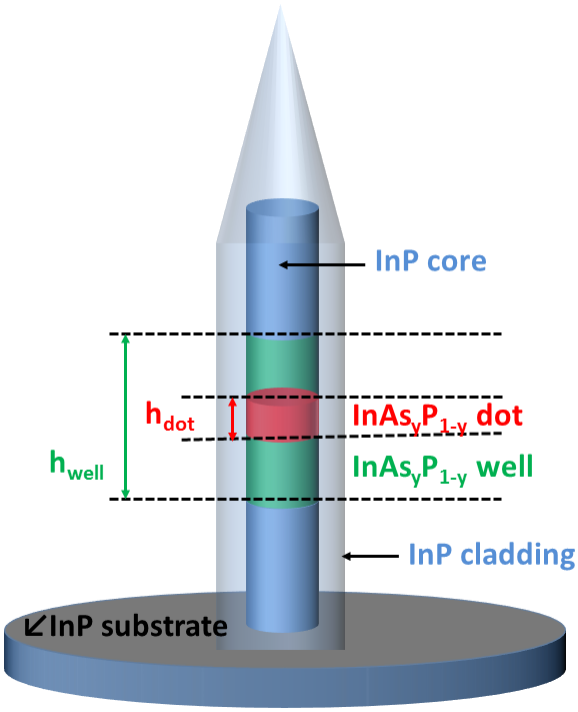

Figure 3.2: Schematic of the QD in a nanowire, courtesy of Dr.Shazzad Rassel

excited state is the p state in both the conduction and valence bands for heights 4-6 nm, so while the energy spacing of the virtual interaction stays the same, a decrease of the height of the QD leads to an increased strength of the QD-phonon coupling. In the range of 7-12 nm, the first excited state is the p state in the conduction band and n_z=2,m=0 state in the valence band, thus leading to the eventual slight increase in the FWHM of the ZPL. This example shows the complex interplay in the QD energy spacings and QD size which governs the QD-phonon coupling strength and is clearly an important consideration. The comparison of the spectra under variation of the radius and height of the QD at 100 K and including both LA and LO phonons are shown in Fig. 3.5. The thickness of the well was kept fixed at 11 nm. The radius has a larger effect on the linewidth than the height. There are oscillations in the FWHM as a function of the radius, when there's an energy spacing in resonance with the LO phonon energy. Around 8-9nm the peak occurs because the m=1 state in the VB is in resonance with the LO phonon energy. Around 11nm it's the m=1 state in CB. At around 14 nm the peak is due to the $n_z = 1, m = 0, n_r = 2$ state in the VB. The 3 orders of magnitude difference in the linewidth from structural variation clearly indicates its importance in the design.

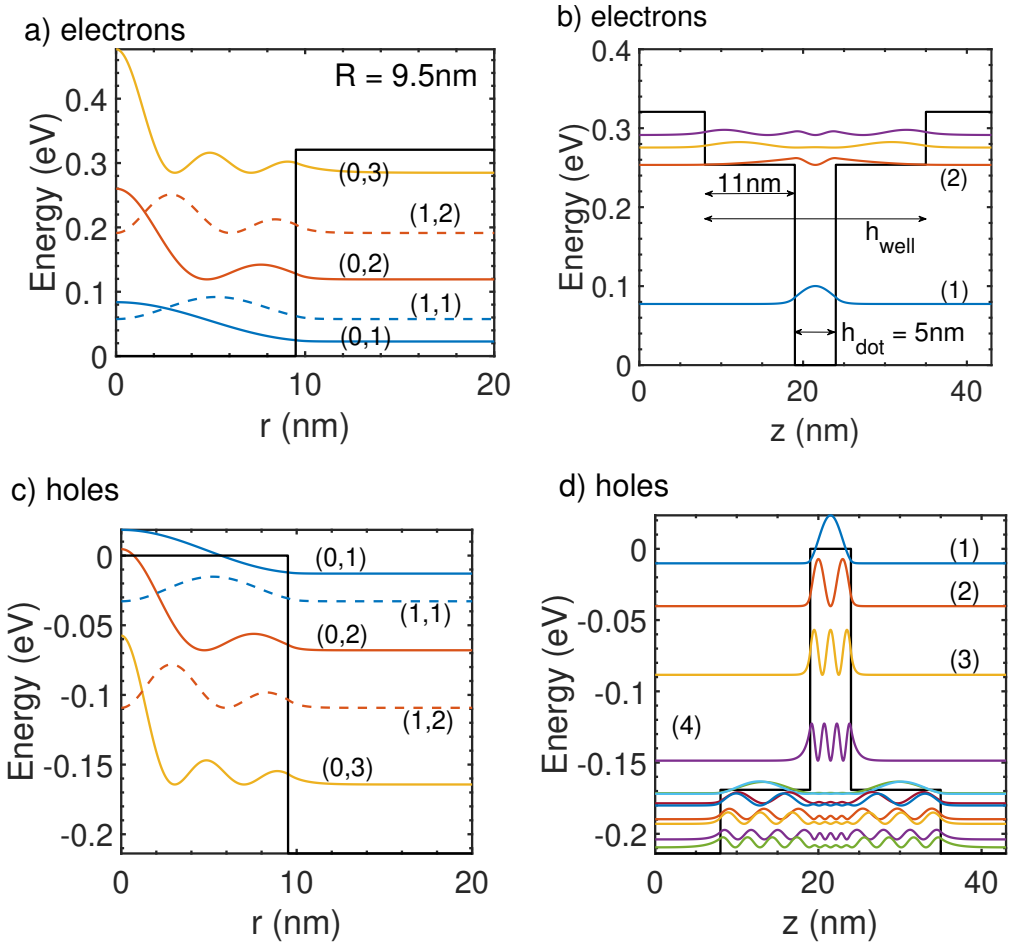

Figure 3.3: Calculated electron/hole wavefunctions in the conduction and valence bands. (a) Electron wavefunctions in the radial direction; (b) electron wavefunctions in the z direction; (c) hole wavefunctions in the radial direction; (d) hole wavefunctions in the z direction. For the radial component m=0 is shown in solid lines and m=1 is shown in dashed lines. The quantum numbers (m, n_r) in the radial direction, and (n_z) are indicated by the numbers in the brackets

In connection to other works, typically the QD wavefunctions have been modeled by spherical Gaussian wavefunctions, which simplifies down to an easy to implement equation [14, 58].

$$\gamma_P = \frac{\alpha\mu}{v_c^4}\int v^{10}e^{-2v^2/v_c^2}n(v)(n(v)+1)dv \tag{3.38}$$

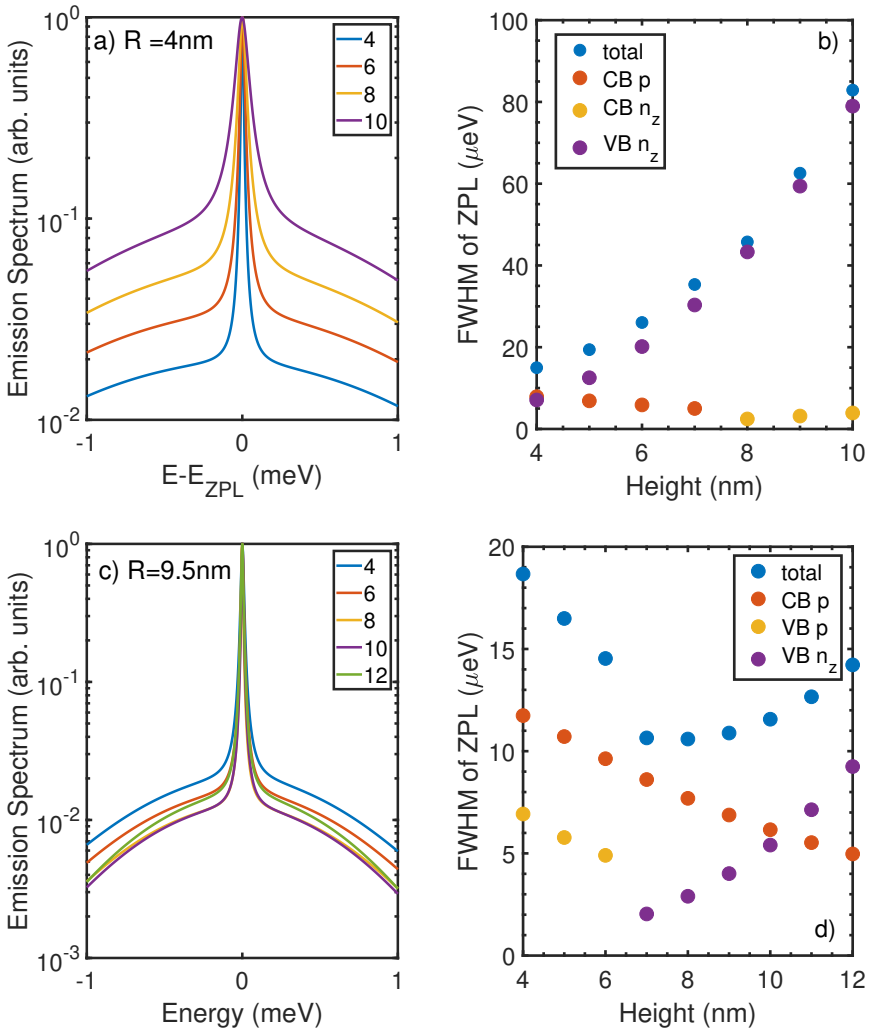

Figure 3.4: Simulated linewidth broadening at T=100 K, where the ZPL broadening is entirely due to phonon interactions (e.g., radiative broadening and other mechanisms are neglected). (a) Emission spectra for QD of radius 4 nm and various heights as indicated in the legend in nm. (b) ZPL broadening for radius of 4 nm and various heights. (c) Emission spectra for QD of radius 9.5 nm and various heights indicated in the legend. (d) ZPL broadening for radius of 9.5 nm and various heights. The labeling CB represents the conduction band and VB represents the valence band. "total" gives the sum of the CB and VB contributions plotted.

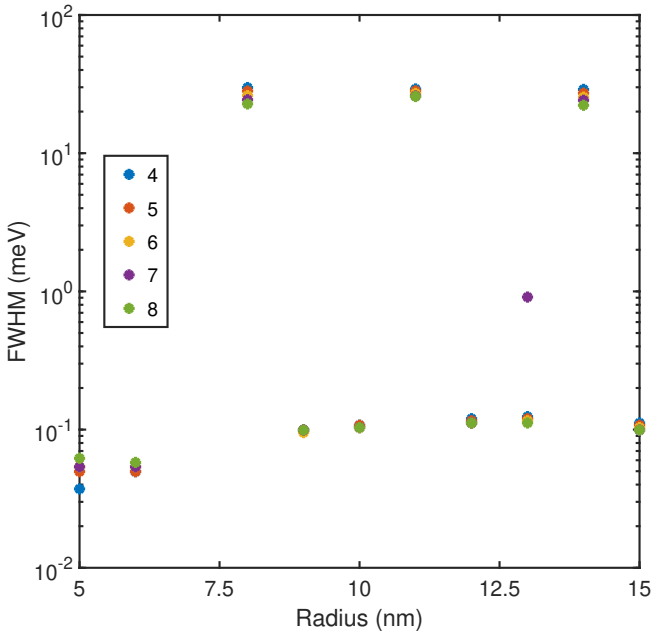

Figure 3.5: Total FWHM including the LO phonon interactions. At T=100K, assuming LO phonon lifetime of 5ps.

It was found that the approach in this work is generally consistent with the Gaussian model, for the lowest energy spacings, if one finds wavefunctions such that the energy spacings are the same. A comparison of the linewidths calculated from both models are show in Figure 3.6, where reference data are from [58]. The energy spacings from spherical geometry is given by $\frac{\hbar^2}{d^2 m^*}$, where d is the spatial confinement length of the QD and m^* is the effective mass. Using the same effective masses as the reference, for $d = 10$nm, the energy spacings are 11.37meV and 1.49meV for the conduction and valence bands respectively. In the quantum disk wavefunctions model, structures were found to match those energy spacings of the spherical model. In the valence band, a 20nm radius and 36nm height were used, and for the conduction band 17nm radius and 31nm height were used. The two models show roughly the same dependence on the temperature – since both equations were derived using the quadratic cumulant to the second order in time. This numerical experiment suggests that for eigen state pairs with the same energy spacing, the coupling strength to LA phonons is approximately the same.

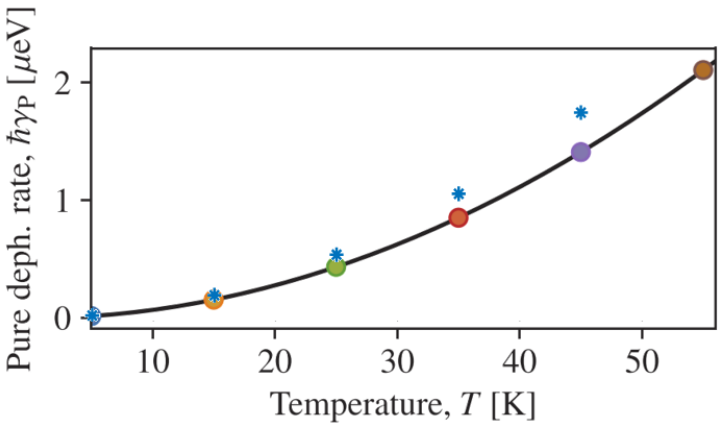

Figure 3.6: Comparison of the results from the spherical Gaussian wavefunctions model (black solid line and circles – reproduced from [58]), and the Quantum disk-like wavefunctions in this thesis (blue stars). The LA phonon material parameters used are the same as that from Ref [58].

3.5.2 Comparison to Experiment

The simulation results are compared to experiment. It was found that LA phonons alone cannot describe the trend in the linewidth broadening with respect to the temperature – LO phonons are required to match to the higher temperature data. The spontaneous emission plus non-radiative recombination rates should be negligible. In Ref [59], the shortest exciton lifetime measured at 10K is around 0.33μeV.

A QD height of 5 nm, radius of 9.5 nm, and well thickness of 11 nm was used in the simulations (see Figure 3.3 for the band structure). A slightly larger radius of 9.5 nm (instead of the targeted experimental value of R=9 nm) was employed as to better match to the experimentally obtained *sp* energy spacing (see Figure 3.9 in Appendix 3.8). Energy spacings of of 35 and 20 meV are calculated in the conduction and valence bands respectively for the *sp* spacings. Figure 3.7 shows comparison of the simulated and experimental spectra at 100-nW excitation power. The experimental data was shifted such that the emission peak is at zero energy detuning (ZPL peak). The experimental resolution was taken into account through convolution of the simulated data with a Gaussian lineshape of 170μeV FWHM - meaning that the new spectrum taking into account the resolution is $S'(\omega) = \int d\omega' S(\omega') L(\omega - \omega')$, where L is a Gaussian function with peak at ω'. A good match of the general lineshape to the experimental is found at all temperatures.

Figure 3.8(a) shows the simulated temperature behaviour of the FWHM of the ZPL. The orange curve shows that the calculated points have a $N_q(N_q + 1)$ dependence on the temperature. Here a small energy for N_q (2 meV) is used, multiplied with a scaling constant to fit the data. Figure 3.8 (b) shows the comparison of the simulated FWHM of the total spectrum, taking into account the experimental resolution, to the experimental FWHM from three different samples. Multiple data points are from different excitation powers.

In connection to other experimental results, the correct order of magnitude and trends are obtained. Typically the experimental data have been fit with a single phonon activation model $\gamma_0 + \gamma_1 \frac{1}{e^{E_1/k_B T} - 1} + \gamma_2 \frac{1}{e^{E_2/k_B T} - 1}$ dependence, where γ_0 is the linewidth broadening at 0K, $\gamma_{1,2}$ is indicative of the exciton-phonon coupling strength, and $E_{1,2}$ is an activation energy [7, 60]. In our model, the $N_q(N_q + 1)$ factor is representative of the underlying physical mechanism of K_Q - the product of phonons being absorbed N_q and the phonons being emitted $N_q + 1$. This is also the variance of the phonon distribution.

3.6 Conclusions

In summary, theory on the optical lineshape broadened by LA and LO phonon interactions was presented for QDs of cylindrical geometry in this Chapter. Analytical formulae were derived accounting for both the broadband and ZPL. For the calculations, the QD radius and height were varied, demonstrating the possibility for optimization of the QD shape to mitigate the linewidth broadening by three orders of magnitude. To reconcile with the widely used spherical wavefunctions model for QDs, it was found that similar ZPL broadening is obtained for LA phonons if wavefunctions are found such that the energy

spacings from both models are the same. Hence, it is recommended that more attention should be paid in matching to the experimental energy spacings.

Given the large uncertainly in many simulation parameters such as the effective mass, band offsets, and LA phonon parameters, our study concludes that the trends obtained are in reasonable agreement with the experimental PL spectra. The PL spectra are of high quality single dots, with low charge noise – which compared to previous literature allows us to really probe the fundamental linewidth broadening due to decoherence from phonons. The model is useful in providing guidelines for future wavefunction engineering of QDs in a wide range of optoelectronic devices.

3.7 Appendix: Evaluation of the form factors

The form factors are evaluated following [34]. The phonon plane wave can be written in cylindrical coordinates using the Jacobi-anger expansion,

$$e^{i\vec{q}\cdot\vec{r}} = e^{iq_z z} \sum_{n=-\infty}^{\infty} i^n J_n(q_r r) e^{in(\theta-\phi_q)} \tag{3.39}$$

where J_n is the Bessel function of the first kind of order n, q_z, q_r and ϕ_q are the z, radial and angle coordinates of the phonon wavevector respectively.

Then substituting the total wavefunction $\psi = \frac{1}{\sqrt{2\pi}} Z(z)R(r)e^{im\theta}$ into the form factor, and using cylindrical coordinates yield

$$\begin{aligned}
\int d^3r \psi_1^* e^{i\vec{q}\cdot\vec{r}} \psi_2 &= \frac{1}{2\pi} \int_{-\infty}^{+\infty} dz \int_0^{\infty} dr r \int_0^{2\pi} d\theta Z_1 Z_2 R_1 R_2 e^{i(m_2-m_1)\theta} e^{iq_z z} \sum_{n=-\infty}^{+\infty} i^{-n} J_n(q_r r) e^{in(\theta-\theta_{\vec{q}})} \\
&= \frac{i^{-n}}{2\pi} \int_{-\infty}^{+\infty} dz e^{iq_z z} Z_1 Z_2 \int_0^{\infty} dr r R_1 R_2 J_n(q_r r) \int_0^{2\pi} d\theta e^{-in\theta_{\vec{q}}} \\
&= i^{-n} e^{-in\theta_{\vec{q}}} \int_{-\infty}^{+\infty} dz e^{iq_z z} Z_1 Z_2 \int_0^{\infty} dr r R_1 R_2 J_n(q_r r)
\end{aligned} \tag{3.40}$$

where it is assumed that the only n that is kept is $n = m_1 - m_2$ from conservation of angular momentum. For K_L, then $n = 0$.

In regards to the Bloch part of the wavefunction, the relation that

$$\int dr^3 u_c^* \psi_c^* e^{i\vec{q}\cdot\vec{r}} u_c \psi_c \approx \int dr^3 u_c^* u_c \int dr^3 \psi_c^* e^{i\vec{q}\cdot\vec{r}} \psi_c, \tag{3.41}$$

Table 3.1: Parameters used for simulated structures

Parameter	Expression/Value	Ref.
Electron effective mass of InP in units of m0	$m_e(r) = 0.1183$, $m_e(z) = 0.0947$	[61]
Electron effective mass of InAs in units of m0	$m_e(r) = 0.0416$, $m_e(z) = 0.037$	[61]
Heavy hole effective mass of InP in units of m0	$m_{hh}(r) = 0.2091$, $m_{hh}(z) = 1.0646$	[61]
Heavy hole effective mass of InAs in units of m0	$m_{hh}(r) = 0.0795$, $m_{hh}(z) = 0.9738$	[61]
Band gap of InP	1.49eV	[62]
Band gap of InAs	0.481eV	[63]
Band gap	$\mathrm{E}_g(\mathrm{InAsP}) = 1.49 + (0.481 - 1.49 - c)x + cx^2$	[64]
bowing parameter	$c = 0.12$eV	[64]
Conduction band offset	0.6dEg	*
Valence band offset	0.4dEg	*
Deformation Potentials	$\mathrm{D}_c = -12.6$eV, $\mathrm{D}_v = -7.1$eV	*
Material density	$\rho_M = 5.667\mathrm{g/cm}^3$	[65, 11]
Speed of sound	$u_s = 4200$m/s	*
LO phonon energy	$\hbar\omega_{LO} = 28$meV	[66]
static permittivity	$\epsilon_s = 15.15\epsilon_0$	[67]
high frequency permittivity	$\epsilon_\infty = 12.3\epsilon_0$	[67]

is used, since the envelope functions are more slowly varying.

3.8 Appendix: Simulation parameters

Table 3.1 lists the simulation parameters used for the interband simulations, and the items with * for the references are justified in this Appendix. There is no general consensus on the conduction and valence band offsets in the literature; these values are complicated by the strain, size, as well as the crystal structure type. These have varied from 0.32 to 0.75 for the fraction of conduction band offset [68, 64, 69]. However our calculated energy spacings are within the expected range - experimental PL data at 180 K shows another peak that is 54meV higher than the main peak (see Fig. 3.9), which should be corresponding to the p exciton. Our calculated p peak is 55 meV higher than main transition, which is in

good agreement to the experimental. In evaluating K_Q the states with the smallest energy differences from the first eigenenergy state should be taken into account, up to a certain cutoff in energy. Only the first excited states are taken into account for the K_Q term due to LA phonons while a few are included for LO phonons. The energy gap for $InAs_{0.5}P_{0.5}$ from our calculation is 955.5meV, which results in an emission energy too high compared to the experimental - however the exact value of the transition energy is not the focus of this work and any energy shifts from the phonon interaction are ignored anyways.

Regarding the phonon simulation parameters, for comparison the phonon coupling parameter often cited in literature [21], $\alpha_p = \frac{(D_c - D_v)^2}{4\pi^2 \hbar u_s^5 \rho_M}$ here would be 0.025ps^2. It has also been previously mentioned that the longitudinal sound velocity in QDs should be smaller than that of the bulk [65], which has a significant effect on the final lineshape due to the factors of $1/u_s^4$ and $1/u_s^8$ in K_L and K_Q respectively. Values of 2960 to 4600m/s have been reported in the literature [65, 70, 11, 71]. Note that values of Dc=-13.6eV and Dv=-7.1eV were used in [11], and Dc = -5.08eV and Dv = -1eV were used in [70]. It is possible to obtain similar spectra using different sets of (D_c,D_v,u_s). The LO phonon energy is expected to be around 27-29meV, and was decided upon through fitting to the experimental results.

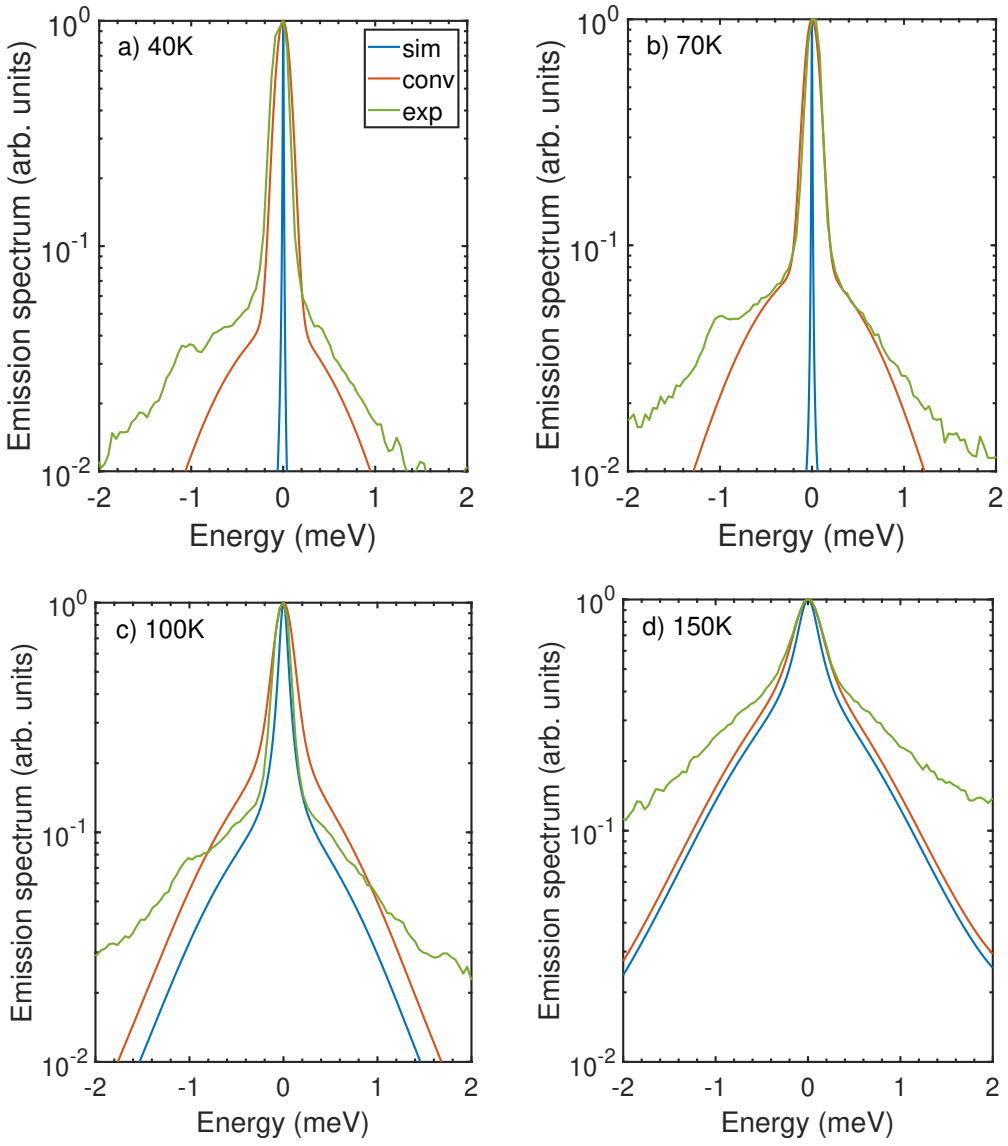

Figure 3.7: Comparison of the experimental and simulated emissions spectra at (a) 40 K, (b) 70 K, (c) 100 K, and (d) 150 K. The blue curve is the as simulated spectrum (labeled as "sim"), orange is the simulated spectrum convolved with 170 μeV spectrometer resolution (labeled as "conv"), and green curve is the experimental data ("exp"). LO phonons at 40 and 70K were not included, because it is expected to be not significant at these low temperatures, and the LO phonon lifetime is a fitting parameter. 7ps was used for the LO phonon lifetime. Experimental data are from the National Research Council.

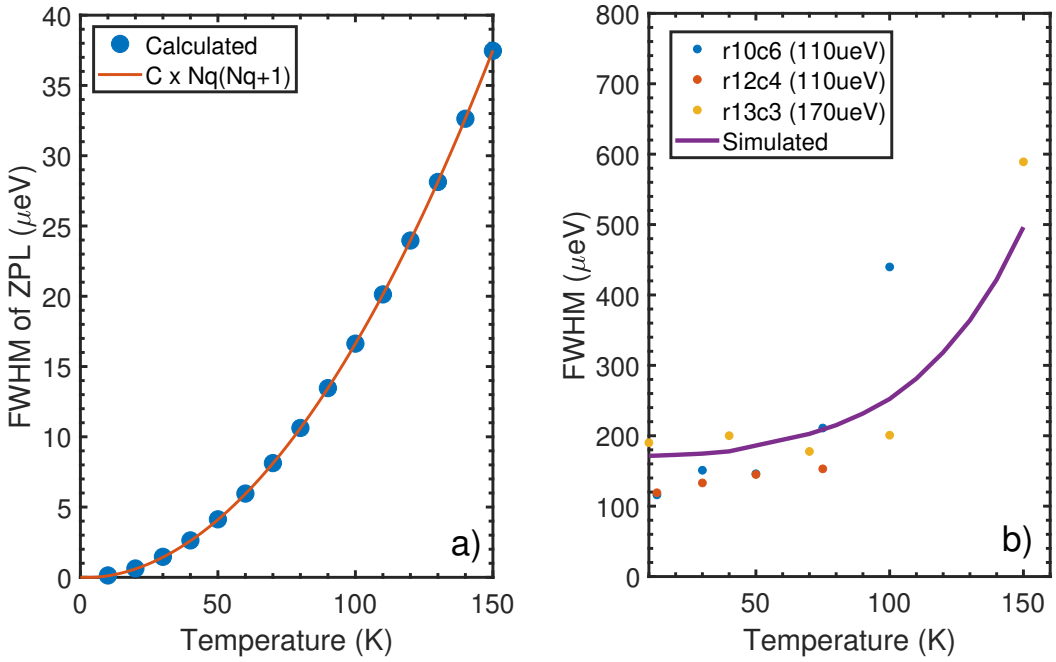

Figure 3.8: (a) Simulated FWHM of the ZPL as a function of temperature. (b) Comparison of the simulated FWHM of the whole spectrum (with the experimental resolution taken into account) to the experimental data with different excitation powers, as a function of temperature. The r10c6, r12c4, r13c3 are the the names of the different samples, provided by our collaborators at the National Research Council. The number in bracket indicate the estimated experimental resolution of the experimental data. The simulation is convolved with 170μeV resolution. Note that LO phonons were excluded for temperatures lower than 50K.

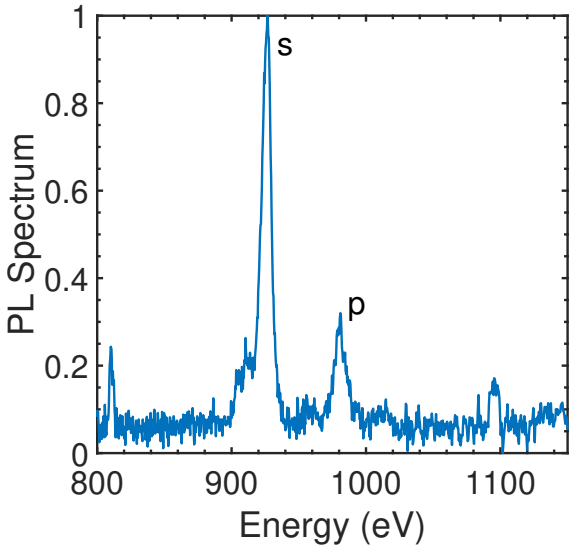

Figure 3.9: Experimental PL spectrum at 180K, recorded with 150 lines and 1s integration. Experimental data from the National Research Council.

Chapter 4

Intersublevel Dynamics

In the intersublevel regime, the application of quantum dots towards the realization of a THz quantum cascade laser (quantum dot cascade laser, QDCL) is investigated. This section begins by presenting a background on the QDCL – how it works, and what are the prospects and challenges for this device. Then the dynamical method that is used to model this type of laser is explained, and finally the simulation results are presented.

4.1 Introduction to quantum dot cascade lasers

The main problem in THz QCL research that researchers are trying to solve is the issue of high temperature operation, and this is important as it would be easier for these kind of lasers to enter the consumer market. Obviously, the higher the operating temperature the better and the ideal laser should operate at room temperature with high output powers. Intermediate milestones towards room temperature operation would include going from liquid nitrogen temperatures to those obtainable by thermoelectric coolers. Since the cryogenics are eliminated, then there's more device mobility and less mechanical vibrations which may help in some optical setups. Thermoelectric cooling setups have been developed recently in Refs. [72, 73].

The current maximum operating temperature is 210K, and has only been slowly improving as of recent years (200K in 2012 and 210K in 2019). In these traditional well-based QCLs, the presence of subbands and continuum of states means that there are lots of decoherence and non-radiative losses, and thermally activated LO phonon emission processes – such as thermal backfilling of the lower laser state. This is the current consensus for

the main mechanism limiting the high temperature operation in traditional THz QCLs. State lifetimes are on the order of sub-ps or ps, linewidth broadening is high at room temperatures, and there are many parasitic transitions to take care of.

The quantum dot cascade laser (QDCL) provides promise that room temperature lasing at THz frequency could be reached. Operating principles of a QDCL is the same as a traditional well based QCL, except the gain medium will be replaced with the nanowires (see Figure 4.1), which offer advantages due to the additional quantum confinement. There is a top electrode and bottom electrode, which also serve as waveguides. The light is emitted from the front facet, similar to a typical ridge laser. The gap space will have to be filled with a low loss material.

Due to the additional confinement in QDs, there is an absence of continuum of states. Intuitively one would think that this would lead to longer state lifetimes. For instance, if the energy spacing between two states is detuned from the LO phonon energy, then the energy conservation requirement cannot be satisfied and, according to Fermi's Golden rule, the transition cannot take place – this is what is referred to as a phonon bottleneck. However, despite this discrete density of states, there is also stronger e-phonon interactions. The smaller the quantum dot, the stronger coupling strength with phonons, which leads to coherent interactions. This is especially true for LO phonons as they have a continuum of the same energy (meaning that each of the different wavevector states have the same energy), which increases the coupling strength. This needs a special treatment, beyond what is described by Fermi's Golden rule. Nevertheless, Zibik et al have measured ultra-long lifetimes of 1.5ns in quantum dots for energy spacings of 14meV, to 2ps for energy spacings of 30meV at 10K [74]. The concept of using more confinement also include using a magnetic field, which was successfully demonstrated to increase the Tmax (maximum operating temperature) of a QCL to 225K using a field strength of 19T [75].

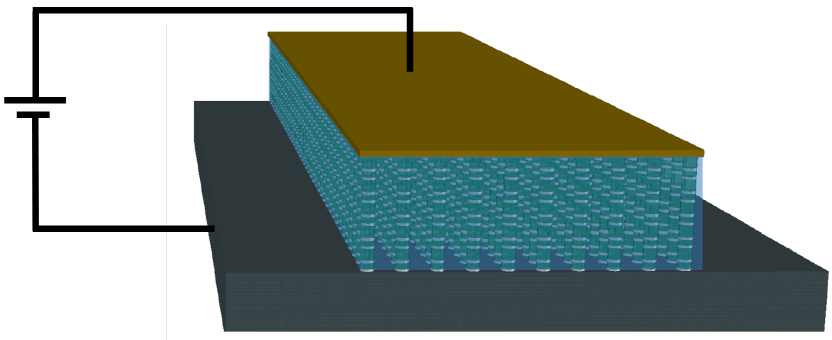

Figure 4.1: Schematic of the QDCL device, modified from [34]

On the experimental side, previous attempts at realizations of a QDCL include work presented in Refs. [36, 37], which utilize top-down etching procedures after the MBE growth. It is not easy to obtain a high aspect ratio of the nanowires through etching techniques, however, surface level Fermi pinning may result in smaller effective diameters [36]. There are several other issues with the QDCL approach in general; surface charges, low filling factor of the gain material, and high losses are of concern. The surface charges are present because of dangling bonds. Recombination of surface charges do not hinder the device operation, however the number of electrons contributing to the laser action is reduced, being wasted as current density flowing on the surfaces. Bottom up growth approaches will result in better side-walls, however one can only obtain a few well and barrier layers, which would probably not be enough for the QCL operation. Filling factors of at least 36% should be aimed for, as random lasing in THz frequencies was demonstrated with this filling factor [76]. The space in between the nanowires should be filled with a nonconducting material with low losses in the THz range. One option is to use benzocyclobutene (BCB) along with nanoparticles to tailor the refractive index [76, 77].

Nevertheless a possible model to use for the design of QDCLs is presented, which can be used in the future when the technology has advanced enough to realize this experimentally.

4.2 Transport

In this section the form of the scattering superoperator that is used is derived. First the different models that there are to describe the electronic transport is reviewed and the approach taken is justified. In general when creating a new model, it is important to consider the accuracy needed vs the numerical cost. Possible models to include are NEGF [35, 78], correlation expansion, polaron density matrix [79], quantum master equations (e.g. in Redfield or Lindblad forms), and rate equations. The main feasible options are summarized in Table 4.1. NEGF is obviously the most accurate, because it is resolved in energy and k, as well as taking into account self consistently the lamb shifts due to interations with the environment. However this comes at the cost of numerical complexity. Correlation expansion approaches essentially write equations of motion for correlation terms such as phonon assisted or impurity-assisted density matrices while cutting off the expansion at some order. However this would be too complicated to implement for QCL systems, as it would require too many states. Rate equations do not work for strong coupling phenomena, as they are relying on Fermi's Golden rules and describe irreversible transitions.

This work is using a density matrix method, having the form of Redfield equations. This method has the risk that it may not be valid for strong coupling, because it is a

Table 4.1: Comparison of transport models

Model	**Pros**	**Cons**
NEGF [35]	Valid for all interaction strengths	Numerical complexity
Interaction (this work)	Easy to enumerize	Not valid for strong coupling, however still experimentally relevant
Polaron density matrix [79]	Valid for strong coupling	Difficult to enumerize for many transitions

perturbative approach in nature – in-fact it is cut off at the second order in time. However this approach should still be applicable for the experimentally feasible range of nanowire diameters.

The coupling strengths can be organized depending on the diameter of the nanowire. The smaller the diameter of the nanowire, then the stronger the coupling effects, and the less accurate our model will be (see Figure 4.2). I expect the strong coupling regime to be only relevant for very thin nanowires with less than around 40nm in diameter. This is actually likely to not be experimentally realizable anyways – it would be difficult to etch down to this precision and there won't be enough mechanical stability. For bottom up grown nanowires, it would be very difficult to achieve the precision that MBE systems offer for the well and barrier lengths.

In the regimes of around 40nm to 100nm diameter is where I expect the Interaction model to exhibit an advantage. This model is also easy to enumerize; because a scattering superoperator was derived in indicial form which is simple to put into code. It is a general model applicable for all different QDCL designs. For diameters larger than 100nm, there are enough states in the lateral direction that one can use traditional quantum well simulation models. Of course, the NEGF approach is valid for all regimes. In the literature, there are only the NEGF[35, 78], polaron density matrix [79], and rate equations model [80] which have been used. The contribution of this work is the development and application of a new model to simulate for the transport dynamics in a QDCL. Although the interaction approach is not new, it has not yet been applied to QDCLs.

The next section derives the format of the scattering superoperator.

4.2.1 Scattering superoperator

The derivation follows that of Refs [82, 83, 84].

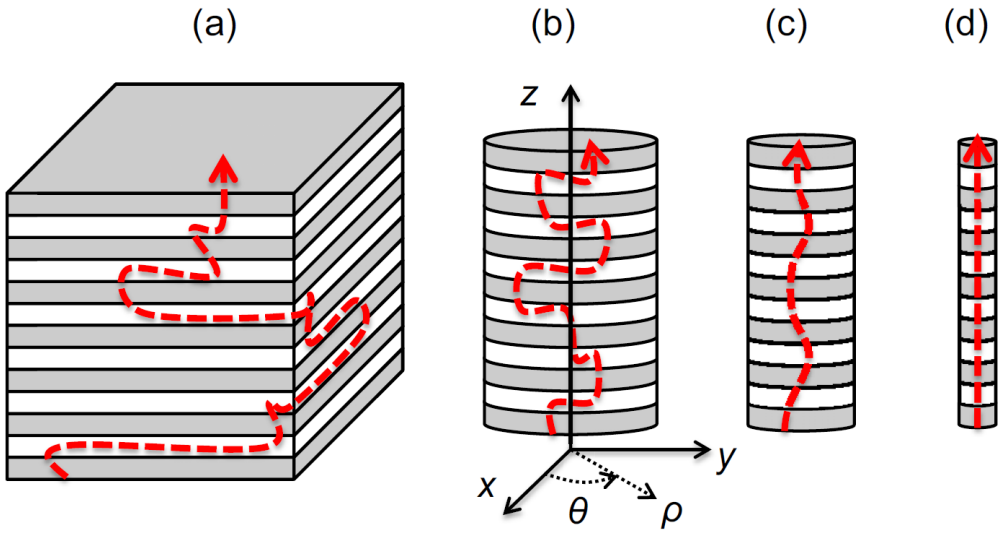

Figure 4.2: Schematic of the different regimes of transport, depending on the diameter of the nanowire. a) > 100nm b) and c) are 40 to 100nm d) < 40nm diameter. The dashed lines represent example paths of electron movement, going from the diffusive regime to ballistic. Reproduced from Ref [81]

.

Let us denote the interaction Hamiltonian in the interaction picture by

$$H_I(t) = \sum_i S_i(t) R_i(t) \tag{4.1}$$

where the S and R denote the system and reservoir operators, and the sum over i is accounting for different kinds of interactions, such as with LA and LO phonons, different q, and with different system states. For example, the reservoir component can be

$$R_q = b_q^\dagger + b_q \tag{4.2}$$

with the system part

$$S_{nm}(q) = M_{nm}(q) \left|n\right\rangle \left\langle m\right| \tag{4.3}$$

Starting with the equation of motion for the reduced density operator, which has used the Markov approximation that $\rho(t') \approx \rho(t)$

$$\frac{d\rho(t)}{dt} = -\frac{1}{\hbar^2} Tr_B \Big\{ \big[H_I(t), \big[\int_0^t dt' H_I(t'), \rho(t)\rho_B \big] \big] \Big\} \tag{4.4}$$

This is valid if the timescale at which ρ changes is slow compared to that of the interaction. The simplification allows for easier numerical implementation, since the time dependence of ρ only depends on its present value.

To transform into the interaction picture, the following is applied:

$$\begin{aligned} S_i(t) &= e^{iH_s t/\hbar} S_i e^{-iH_s t/\hbar} \\ R_i(t) &= e^{iH_r t/\hbar} R_i e^{-iH_r t/\hbar}. \end{aligned} \tag{4.5}$$

Physically, by using the interaction picture the time evolution arising from H_0 is separated from that of the interaction Hamiltonians. The sum over the wavevectors q is dropped for now. Then plugging these into the integro-differential form of the equations of motion yields

$$\begin{aligned} \frac{d\rho(t)}{dt} &= \frac{-1}{\hbar^2} Tr_B\{[S(t)R(t), [\int_0^t dt' S(t')R(t'), \rho(t)\rho_B]]\} \\ &= \frac{-1}{\hbar^2} \int_0^t dt' Tr_B\{R(t)R(t')\rho_B\} S(t)S(t')\rho(t) - Tr_B\{R(t)\rho_B R(t')\} S(t)\rho(t)S(t') \\ &- Tr_B\{R(t')\rho_B R(t)\} S(t')\rho(t)S(t) + Tr_B\{\rho_B R(t')R(t)\}\rho(t)S(t')S(t) \end{aligned} \tag{4.6}$$

To transform back to the Schrodinger picture, $e^{-iHt/\hbar} X e^{iHt/\hbar}$ is applied to obtain

$$\frac{d\rho}{dt} = \frac{1}{i\hbar}[H_0, \rho] + \Gamma(t)\rho(t) \tag{4.7}$$

where

$$\begin{aligned} \Gamma(t)\rho(t) = \frac{-1}{\hbar^2} \int_0^t d\tau Tr_B\{Re^{-iH_r\tau/\hbar} Re^{iH_r\tau/\hbar}\rho_B\} Se^{-iH_s\tau/\hbar} Se^{iH_s\tau/\hbar}\rho(t) \\ - Tr_B\{R\rho_B e^{-iH_r\tau/\hbar} Re^{iH_r\tau/\hbar}\} S\rho(t)e^{-iH_s\tau/\hbar} Se^{iH_s\tau/\hbar} \\ - Tr_B\{e^{-iH_r\tau/\hbar} Re^{iH_r\tau/\hbar}\rho_B R\} e^{-iH_s\tau/\hbar} Se^{iH_s\tau/\hbar}\rho(t)S \\ + Tr_B\{\rho_B e^{-iH_r\tau/\hbar} Re^{iH_r\tau/\hbar} R\}\rho(t)e^{-iH_s\tau/\hbar} Se^{iH_s\tau/\hbar} S \end{aligned} \tag{4.8}$$

where I let $\tau = t - t'$. It was assumed that the system and reservoir operators commute with eachother but not necessarily between themselves. The next step is to carry out the trace over the bath, from which the density matrix of the target electronic system (i.e. reduced density matrix) is obtained. And in doing so, it is assumed that the bath is large such that it remains in thermal equilibrium, despite the interactions with the system.

Making use of the invariance of the trace from cyclic permutation, I obtain

$$\begin{aligned}\Gamma(t)\rho(t) = \frac{-1}{\hbar^2}\int_0^t d\tau \sum_{\pm} e^{\mp i\omega_q\tau}(N_q + \frac{1}{2} \pm \frac{1}{2})[Se^{-iH_s\tau/\hbar}Se^{iH_s\tau/\hbar}\rho(t)] \\ - \sum_{\pm} e^{\pm i\omega_q\tau}(N_q + \frac{1}{2} \pm \frac{1}{2})[S\rho(t)e^{-iH_s\tau/\hbar}Se^{iH_s\tau/\hbar}] \\ - \sum_{\pm} e^{\mp i\omega_q\tau}(N_q + \frac{1}{2} \pm \frac{1}{2})[e^{-iH_s\tau/\hbar}Se^{iH_s\tau/\hbar}\rho(t)S] \\ + \sum_{\pm} e^{\pm i\omega_q\tau}(N_q + \frac{1}{2} \pm \frac{1}{2})[\rho(t)e^{-iH_s\tau/\hbar}Se^{iH_s\tau/\hbar}S]\end{aligned} \tag{4.9}$$

Now in order to implement this in code, the above is written in indexing notation

$$\begin{aligned}\Big[\Gamma(t)\rho(t)\Big]_{ab} = \frac{-1}{\hbar^2}\int_0^t d\tau \sum_{\pm} e^{\mp i\omega_q\tau}(N_q + \frac{1}{2} \pm \frac{1}{2})[S_{ac}(e^{-iH_s\tau/\hbar}S_ie^{iH_s\tau/\hbar})_{cd}\rho_{db}(t)] \\ - \sum_{\pm} e^{\pm i\omega_q\tau}(N_q + \frac{1}{2} \pm \frac{1}{2})[S_{ac}\rho_{cd}(t)(e^{-iH_s\tau/\hbar}S_ie^{iH_s\tau/\hbar})_{db}] \\ - \sum_{\pm} e^{\mp i\omega_q\tau}(N_q + \frac{1}{2} \pm \frac{1}{2})[(e^{-iH_s\tau/\hbar}S_ie^{iH_s\tau/\hbar})_{ac}\rho_{cd}(t)S_{db}] \\ + \sum_{\pm} e^{\pm i\omega_q\tau}(N_q + \frac{1}{2} \pm \frac{1}{2})[\rho_{ac}(t)(e^{-iH_s\tau/\hbar}S_ie^{iH_s\tau/\hbar})_{cd}S^s_{db}]\end{aligned} \tag{4.10}$$

This scattering superoperator goes into the time evolution of the density matrix as

$$\frac{d\rho_{ab}}{dt} = \frac{1}{i\hbar}[H_0, \rho]_{ab} + \Big(\Gamma(t)\rho(t)\Big)_{ab} \tag{4.11}$$

This scattering superoperator is describing the incoherent time evolution of ρ_{ab} due to interactions with other ρ mediated by Γ. Terms like $(e^{-iH_s\tau/\hbar}S_ie^{iH_s\tau/\hbar})_{cd}$ are evaluated as

$$\begin{aligned}&e^{-i\sum_i \omega_i|i\rangle\langle i|\tau}\,|c\rangle\,\langle d|\,e^{i\sum_i \omega_i|i\rangle\langle i|\tau} \\ &= e^{-i\omega_c\tau}\,|c\rangle\,\langle d|\,e^{i\omega_d\tau} \\ &= |c\rangle\,\langle d|\,e^{i\omega_{dc}\tau}\end{aligned} \tag{4.12}$$

Now I let $S_{ab}S_{cd} = V_{ab,cd}$ to be consistent/compare to the equations in [85]. Putting

everything together,

$$\begin{aligned}\Big(\Gamma(t)\rho(t)\Big)_{ab} = \frac{-1}{\hbar^2}\int_0^t d\tau \sum_{\pm} e^{\mp i\omega_q\tau}(N_q+\frac{1}{2}\pm\frac{1}{2})[V_{ac,cd}e^{i\omega_{dc}\tau}\rho_{db}(t)] \\ -\sum_{\pm} e^{\pm i\omega_q\tau}(N_q+\frac{1}{2}\pm\frac{1}{2})[V_{ac,db}\rho_{cd}(t)e^{i\omega_{bd}\tau}] \\ -\sum_{\pm} e^{\mp i\omega_q\tau}(N_q+\frac{1}{2}\pm\frac{1}{2})[V_{ac,db}e^{i\omega_{ca}\tau}\rho_{cd}(t)] \\ +\sum_{\pm} e^{\pm i\omega_q\tau}(N_q+\frac{1}{2}\pm\frac{1}{2})[\rho_{ac}(t)V_{cd,db}e^{i\omega_{dc}\tau}]\end{aligned} \tag{4.13}$$

Next, it is desirable to write the whole equation in terms of ρ_{cd}. The last two terms become

$$V_{cddb}e^{i\omega_{dc}\tau}\rho_{ac} = \delta_{ac}\sum_f V_{dffb}e^{i\omega_{fd}\tau}\rho_{cd} \tag{4.14}$$

and

$$V_{accd}e^{i\omega_{dc}\tau}\rho_{db} = \delta_{bd}\sum_f V_{affc}e^{i\omega_{cf}\tau}\rho_{cd} \tag{4.15}$$

To summarize, the final equation is

$$\begin{aligned}\Gamma_{ab,cd}(t)\rho_{cd}(t) = \frac{1}{\hbar^2}\sum_{\pm}(N_q+\frac{1}{2}\pm\frac{1}{2})\Big[\int_0^t d\tau V_{ac,db}e^{i(\omega_{ca}\mp\omega_q)\tau}\rho(t)_{cd} + \int_0^t d\tau V_{ac,db}e^{i(\omega_{bd}\pm\omega_q)\tau}\rho(t)_{cd} \\ -\delta_{bd}\sum_f\int_0^t d\tau V_{af,fc}e^{i(\omega_{cf}\mp\omega_q)\tau}\rho(t)_{cd} - \delta_{ac}\sum_f\int_0^t d\tau V_{df,fb}e^{i(\omega_{fd}\pm\omega_q)\tau}\rho(t)_{cd}\Big]\end{aligned} \tag{4.16}$$

Note that this is the same format as the interaction approach in Ref [85] when taken to the long time limit.

To illustrate what this scattering superoperator does, it is shown below that it does reduce down to simpler models. For example, after taking the long time limit, I find by

construction for the occupation dynamics:

$$\begin{aligned}
\frac{dn_a}{dt} &= \sum_{cd} \Gamma_{aa,cd}\rho_{cd} \\
&\approx \sum_{cc} \Gamma_{aa,cc}\rho_{cc} \\
&= \sum_{c} V_{ac,ca}(\delta(E_a - E_c) + \delta(E_a - E_c))\rho_{cc} \\
&- \sum_{c}\sum_{f} \Big[\delta_{a,c}V_{cf,fa}\delta(E_f - E_c) + \delta_{a,c}V_{af,fc}\delta(E_f - E_c)\Big]\rho_{cc} \\
&= \sum_{c} 2V_{ac,ca}\delta(E_a - E_c)\rho_{cc} - \sum_{f}\Big[2V_{af,fa}\delta(E_f - E_a)\Big]\rho_{aa} \\
&= \sum_{c} R_{c\to a}n_c - \sum_{c} R_{a\to c}n_a.
\end{aligned} \tag{4.17}$$

where the $\delta(E_{\text{final}} - E_{\text{initial}})$ denotes the energy conservation. This is the same as rate equations, that the time evolution of populations in state a is the sum of that coming into state a minus that going out. For the lifetime of a coherence it is found that:

$$\begin{aligned}
\Gamma_{ab,ab} &= 2V_{aa,bb} - \sum_{f}\Big[V_{bf,fb}\delta(E_f - E_b) + V_{af,fa}\delta(E_f - E_a)\Big] \\
&= 2V_{aa,bb} - V_{bb,bb} - V_{aa,aa} - \sum_{f\neq b,a}\Big[V_{bf,fb}\delta(E_f - E_b) + V_{af,fa}\delta(E_f - E_a)\Big] \\
&= 2V_{aa,bb} - V_{bb,bb} - V_{aa,aa} - \sum_{f\neq b,a}\frac{1}{2}\Big[R_{b\to f} + R_{a\to f}\Big]
\end{aligned} \tag{4.18}$$

Which is half of the level lifetimes, plus another pure dephasing component. Interestingly this is the same as the definition from the commonly used Ando/Unuma [86] model in the QCL community, and this is also the same format as the diagonal electron phonon interaction in the independent boson model (when ignoring the energy shifts). However, in the more commonly used tight binding basis approaches in the THz QCL community, the use of this definition is known to still yield large spikes in the IV curve, which does not match with the experiment. This general lack of dephasing in the previous models is mainly due to the inconsistencies in the choice of basis.

4.2.2 Periodicity

The QCL is composed of hundreds of repeats of the same modules, and obviously, it is not feasible to simulate all of them. Therefore I simulate for one module and use periodic boundary conditions. This affects the format of the density matrix and the scattering superoperator [85], which is explained in this section.

If blocks of density matrices $\rho_{\mu,v}$ are written describing the states in modules μ and v, and only the next nearest neighbours are included,

$$\begin{bmatrix} \dots & & & & \\ \rho_{-1,-2} & \rho_{-1,-1} & \rho_{-1,0} & 0 & 0 \\ 0 & \rho_{0,-1} & \rho_{0,0} & \rho_{0,1} & 0 \\ 0 & 0 & \rho_{1,0} & \rho_{1,1} & \rho_{1,2} \\ & & & & \dots \end{bmatrix} \tag{4.19}$$

then the periodicity means that the values of the density matrix elements in module 0 is the same as that of module -1 and module 1 etc. ($\rho_{0,0} = \rho_{-1,-1} = \rho_{1,1}$). The density matrix elements describing the coherence between modules 0 and -1 is also the same as that describing modules 1 and 0, since the only change is a shift down a module. Thus only the difference between the modules matter, and the notation can then be shortened by using $\rho_{\mu,v} = \rho_{v-\mu}$, to write

$$\begin{bmatrix} \dots & & & & \\ & \rho_0 & \rho_1 & 0 & \\ & \rho_{-1} & \rho_0 & \rho_1 & \\ & 0 & \rho_{-1} & \rho_0 & \\ & & & & \dots \end{bmatrix} \tag{4.20}$$

For the scattering matrix elements however only the shift property applies. To include periodicity in the scattering superoperator, the trick is to sum over the indices of the neighbouring modules, for example $\sigma = -1, 0, 1$ (many thanks to Andrew Pan and Benjamin Burnett for providing notes regarding how to implement the periodicity in their scattering superoperator in [85]). For a $\Gamma_{\substack{AB,CD \\ \mu;\ v}}$ describing the transfer of ρ_{CD} of type v to ρ_{AB} of type μ, this is implemented as

$$\Gamma_{\substack{AB,CD \\ \mu;\ v}} = \sum_{\sigma} \Gamma_{\substack{AB,C\ D \\ 0\ \mu;\ \sigma\ \sigma+v}} \tag{4.21}$$

However in practice, u and v are set to zero, and 3 modules are treated as an effective one module in the simulation. This way, I am only solving for coherences that are extending within one (effective) module but important coherences in the system of equations will not be neglected. In the end, one can take the results from the middle module to compute the observables. Now carrying out the above equation 4.21 with $\mu, v = 0$ the follwing is obtained:

Scattering Superoperator

$$\Gamma_{\substack{AB,CD\\0;\ \ 0}} =$$
$$\sum_{\sigma}\sum_{\pm}(N_q+\frac{1}{2}\pm\frac{1}{2})\Bigg[V_{\substack{AC,DB\\0,\sigma;\ \sigma,0}}\frac{e^{i(\omega_{CA+\sigma U}\mp\omega_q)t}e^{-\gamma t}-1}{i(\omega_{CA+\sigma U}\mp\omega_q)-\gamma}+V_{\substack{AC,DB\\\sigma,0;\ 0,\sigma}}\frac{e^{i(\omega_{BD+\sigma U}\pm\omega_q)t}e^{-\gamma t}-1}{i(\omega_{BD+\sigma U}\pm\omega_q)-\gamma}$$
$$-\delta_{B,D}\sum_F V_{\substack{AF,FC\\\sigma,0;\ 0,\sigma}}\frac{e^{i(\omega_{CF+\sigma U}\mp\omega_q)t}e^{-\gamma t}-1}{i(\omega_{CF+\sigma U}\mp\omega_q)-\gamma}-\delta_{A,C}\sum_F V_{\substack{DF,FB\\0,\sigma;\ \sigma,0}}\frac{e^{i(\omega_{FD+\sigma U}\pm\omega_q)t}e^{-\gamma t}-1}{i(\omega_{FD+\sigma U}\pm\omega_q)-\gamma}\Bigg] \tag{4.22}$$

where γ is the inverse lifetime of the phonon. For LO phonons the lifetime was approximated using $8-\frac{T}{54.5}$ps [34], where T is the temperature. For LA phonons it is assumed that they have infinite lifetime. U is the energy drop per module, and A, B, C, D, F are indices of the states in one module.

Additional pure dephasing can be added into the scattering superoperator. This generally helps with the numerics. Physically additional dephasing is justified by other scattering mechanisms other than LA and LO phonons, as well as virtual interactions. The dephasing contribution is added on by using

$$\Gamma_{AB,CD} = \Gamma_{AB,CD} + \frac{\delta_{A,D}\delta_{B,C}}{\tau^*} - \frac{\delta_{A,C}\delta_{B,D}}{\tau^*} \tag{4.23}$$

where τ^* is a pure dephasing time, and $\delta_{i,j}$ is the kronecker delta.

In reality there may be electrical field domains which break the periodicity, which would cause the different modules to be biased at different voltages. It is expected to be an important factor to consider in the design of QDCLs. Its treatment in traditional QCLs have been investigated in Ref [87]. However that is beyond the scope of this thesis.

4.2.3 Scattering Mechanisms

The specific equations used for the LO and LA phonon scattering for QDCLs is similar to that of the interband case.

For LA phonons,

$$V_{ac,db} = \sum_q \frac{\hbar\omega_q}{2\rho_M u_s^2 V} D_c^2 \int d^3r \psi_a^*(r) e^{iq\cdot r} \psi_c(r) \int d^3r \psi_d^*(r) e^{-iq\cdot r} \psi_b(r) \tag{4.24}$$

For LO phonons,

$$V_{ab,cd} = \sum_q \frac{e^2\hbar\omega_{LO}}{2V\epsilon_0\kappa} \frac{1}{q^2} \int d^3r \psi_a^*(r) e^{iq\cdot r} \psi_b(r) \int d^3r \psi_c^*(r) e^{-iq\cdot r} \psi_d(r) \tag{4.25}$$

To evaluate the form factor component, again, the key is to use the Jacobi-anger expansion which is the same as the interband case (see Appendix 3.7). In the spatial integrals over r, $n_1 = m_a - m_b$ (for $e^{in_1\theta}e^{-im_a\theta}e^{im_b\theta} = 1$), and $n_2 = m_d - m_c$ (for $e^{-in_2\theta}e^{-im_c\theta}e^{im_d\theta} = 1$) have to be satisfied. Then carrying out the sum over phonon wavevectors q,

$$\begin{aligned}
&= \sum_q \Big[\int dr r \int dz Z_a R_a Z_b R_b e^{iq_z z} i^{n_1} J_{n1}(q_r r) e^{in_1(-\phi_q)} \Big] \\
&\quad \times \Big[\int dr r \int dz Z_c R_c Z_d R_d e^{-iq_z z} i^{-n_2} J_{n2}(q_r r) e^{in_2\phi_q} \Big] \\
&= \frac{V}{(2\pi)^3} \int_0^\infty dq_r q_r \int_{-\infty}^\infty dq_z \int_0^{2\pi} d\phi_q \Big[\int dr r \int dz Z_a R_a Z_b R_b e^{iq_z z} i^{n_1} J_{n1}(q_r r) e^{-in_1\phi_q} \Big] \\
&\quad \Big[\int dr r \int dz Z_c R_c Z_d R_d e^{-iq_z z} i^{-n_2} J_{n2}(q_r r) e^{in_2\phi_q} \Big]
\end{aligned} \tag{4.26}$$

Now the integral over ϕ_q will be zero unless if $n_2 - n_1 = 0$, or in other words the selection rule is that $m_a - m_b + m_c - m_d = 0$. The factor of i disappears and all scattering rates are real for the allowed transitions. For the order of the Bessel function, I chose to use $|n|$ according to T.Grange's work [35]

4.2.4 General Remarks and Summary

Some general remarks in the actual implementation of the scattering superoperator are as follows. The imaginary part of occupations are in theory zero, but in practice one will

typically obtain the imaginary part to approximately numerical precision, hence typically if the occupations of the density matrix are sensible then one knows that the scattering superoperator has been implemented correctly. One recommendation is to check for symmetries in the scattering superoperator (e.g. is it of tetradic form). Also note that this scattering superoperator is not in Lindblad form, so it does not guarantee positivity, and it is possible to obtain negative occupation terms which are obviously not physically correct. However, in the Lindblad equations the energy shifts cannot be included.

To summarize, a set of quantum master equations have been derived, accurate to the second order in the Born-Markov approximations. It is fairly intuitive as one can draw connections between this model and the semiclassical rate equations. This model is valid for weak perturbations (e.g. weak e-phonon couplings). When the interaction is strong, this needs e.g. the phonons to be in the system. The main characteristics of this transport model is that it does not have strict energy conserving deltas and the periodicity of the QCL structure is included. Both LO and LA phonons are included, as well as a finite lifetime of LO phonons in the scattering rate. The two-phonon mechanisms (K_Q) can also be accounted for, through a simple addition of time-independent pure dephasing rate.

4.3 Observables

4.3.1 Gain

In this approach the procedure is to introduce the ac electric field

$$E(t) = E_{ac}\cos(\omega t) \tag{4.27}$$

This gives the electron-light interaction Hamiltonian

$$H_{opt}(t) = |e|z_{ij}E_{ac}\cos(\omega t) \tag{4.28}$$

The corresponding gain was calculating through

$$g(\omega) = \frac{|e|\omega N_{3D}}{n_r c\epsilon_0} Im\Big(\frac{P(\omega)}{|E(\omega)|}\Big) \tag{4.29}$$

where

$$\begin{aligned} P(\omega) &= \int dt \rho_{ij} e^{i\omega t} z_{ij} \\ E(\omega) &= \int dt E_{ac}\cos(\omega t) e^{i\omega t} \end{aligned} \tag{4.30}$$

are the polarization and optical field strength in the frequency domain, respectively. In the implementation of this method, it is assumed that the steady state is first established by the scatterings, and then use that as the initial condition for which the ac field is applied.

The advantage of this approach is that there's no need to assume Fourier expansion of frequencies or RWA (as was done in Ref. [85]), or rely on the accuracy or validity of the calculated current densities (as was done in Ref. [51]). The only drawback is that one would have to solve the density matrix equations in time, which may run into divergency issues – especially for strong scattering conditions. The other approach that I have found to be robust, easy to implement, and reliable in the weak lasing field strength regime is Ref. [85]. Both methods are used in this thesis.

4.3.2 Current Density

Options for calculating the current density include using the quantum mechanical probability current which is related to the wavefunctions and the coherence values: $J \propto \rho_{ba}\psi_a^*(z)\frac{\hbar}{im}\frac{\partial\psi_b(z)}{\partial z}$, or using the expectation value of the coherent velocity. The former has the advantage that it may offer a better pictorial view of the underlying transport, however has the drawback that it is spatially varying. Many levels, including those that are quasi-bound and are ill-defined, may have to be included to obtain a converged value. Note that one can also calculate an incoherent current density through defining a velocity scattering superoperator [85], however this is ignored for the QDCL calculation due to the already long calculation time. If done correctly, the incoherent contribution should be small [88], especially so in these quantum dot systems.

In this thesis the expectation value of the coherent current density is used, in which the accuracy only depends on the values of the density matrix elements calculated. The coherent current density is given by

$$\begin{aligned} J &= N_d q \langle v_{coh} \rangle \\ v_{coh} &= \frac{i}{\hbar}[H, z] \end{aligned} \tag{4.31}$$

H is the energy eigenstates Hamiltonian with the eigen-energies on the diagonals, N_d is the 3D doping concentration, and z is the position operator. The expectation value is evaluated as $Tr(\rho v_{coh})$, for the target states.

4.4 Simulation Flow

A schematic of the simulation workflow is shown in Figure 4.3. The simulation is started by inputting the simulation conditions such as the temperature, electric field, doping concentration, materials and quantum design. Then the wavefunctions (eqn 2.6) are calculated. With the wavefunctions one can then calculate the form factors and the scattering matrix elements, this is the time consuming part of the calculation. However these form factors can be stored and re-used at different temperatures. Next the scattering superoperator (eqn 4.22) is constructed, it is sufficient to calculate the scattering superoperator at some arbitrary long enough of a time, and use the matrix inverse to solve for the steady state ρ. When calculating the form factors one should be careful to use fine enough of a discretization for the LA phonon energy, such that it is sufficient for the effective infinite time. Finally, once the scattering superoperator and the entire density matrix is obtained, one can calculate the output characteristics such as the current density (eqn 4.31) and gain (eqn 4.29). The calculation time on a i7-8700K CPU @3.70GHz desktop for one electric field, if starting from scratch, and not including calculation of the gain, is around one hour. The LA phonon scattering is only included for the transport in one module in order to save computation time. The calculation time depends on the number of states that are included – this is for 54 states.

4.5 Results

4.5.1 Original Design

The model is tested on the simplest QDCL design possible, with three states per operation module. The quantum design is shown in Figure 4.4. Starting from the injector barrier, the design layer thicknesses are 3.7/8.2/3.8/16.8 nm GaAs/$Al_{0.2}Ga_{0.8}As$ [79]. It is a two well design; the two well operation scheme has shown record high temperature performance in the traditional quantum well based THz QCL systems [73]. The operation mechanism is as follows: starting from the injector state "I", electrons are injected into the upper lasing state "U". Then through both radiative and non-radiative scattering electrons from state "U" can be transported to state "L" the lower lasing state. The state L is then depopulated through LO phonon scattering to states I and U of the next module. Figure 4.4 b) also shows other sublevels that are present in the in-plane direction.

First the gain spectra at T=0K is shown in Figure 4.5. Only the s states are included. The peak around 12meV is due to the I to L transition and peak around 10meV is due to

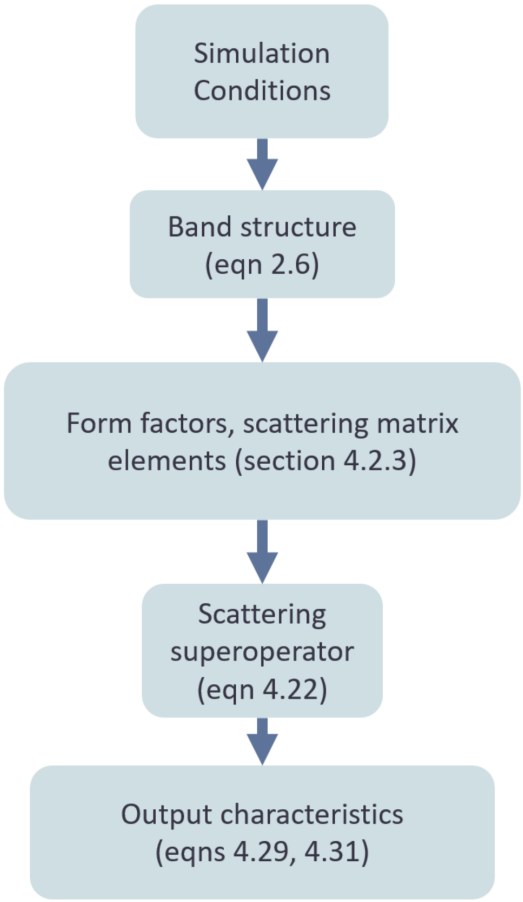

Figure 4.3: Flowchart of the simulation program.

the U to L transition. The absorption peak is due to the U to I transition. To investigate the effect of the different types of phonons on the transport, the LA phonon interactions is turned on and off in the code, while the LO phonon interaction is kept on as this particular lasing mechanism is mainly dependent on this. It was found that the LA phonon emission helps to inject electrons into the upper lasing state – increasing the population from of state U from 0.501 to 0.688. This resulted in a higher peak gain.

Next the effect of the optical field is shown in Figure 4.6, still at T=0K. As expected the gain decreases with increasing field strength, due to increasing stimulated emission which depopulates the upper lasing state. It was also found that due to the stronger interaction of the U to L transition with the optical field, its peak gets reduced down first.

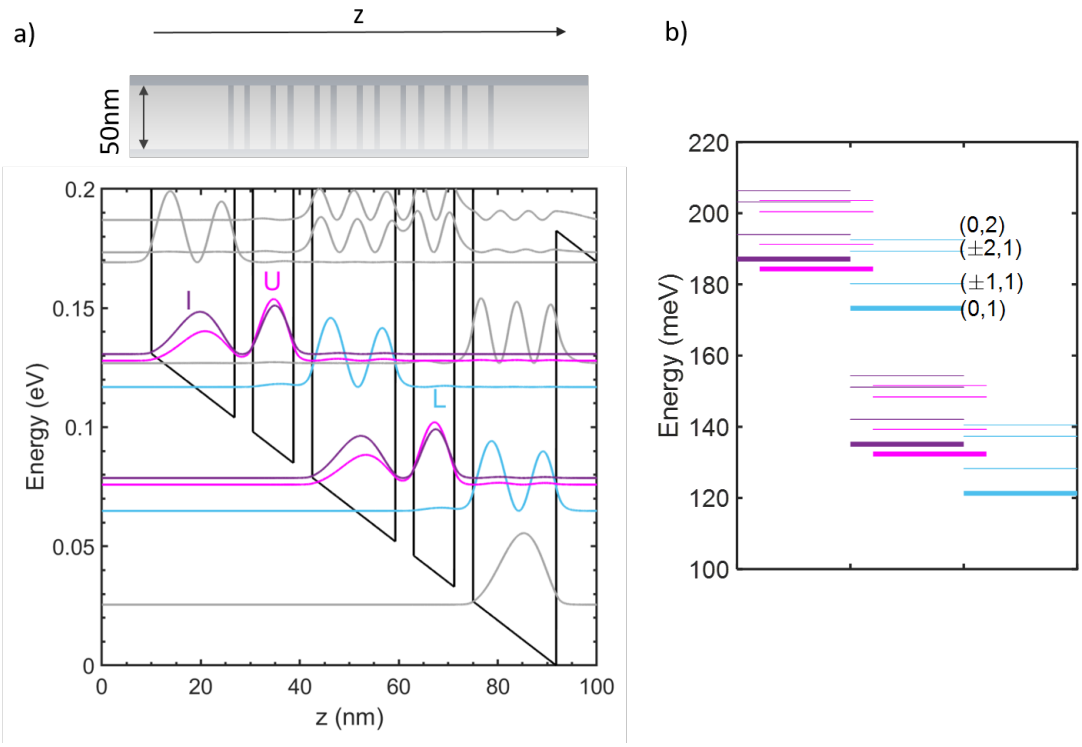

Figure 4.4: a) Schematic of the nanowire (top) and the band structure diagram at electric field of 16kV/cm (bottom) – colored lines indicate the states included in the simulation. b) Simplified energy diagram of a few of the energy levels. The numbers in brackets are (m, n_r). The s state is indicated in thicker lines. The doping concentration was 3.25x10^{10}cm^{-2}.

The effect of with/without LA phonons is then investigated at higher temperatures (50K and 300K) in Figure 4.7. There are 18 states per period that are included: there's the 3 states in the z direction, and each of these have (m,n_r) = (0,1), (±1,1), (±2,1), and (0,2) states – see Figure 4.4 b) for the energy level diagram. This results in a total of 18x3=54 states when effectively treating three modules as one. The energy difference between the lowest and highest intersublevels for the same type of n_z state is 19.2meV.

At both 50K and 300K, there are multiple peaks, which are from all the different intersublevels (e.g. different m, n_r). It is also found that this mechanism of LA phonon assisted injection is less pronounced at higher temperatures, due to the increasing amount of thermal backfilling (LA phonon absorption). The peak positions are different at the different temperatures due to the phonon interactions being stronger at higher temperatures,

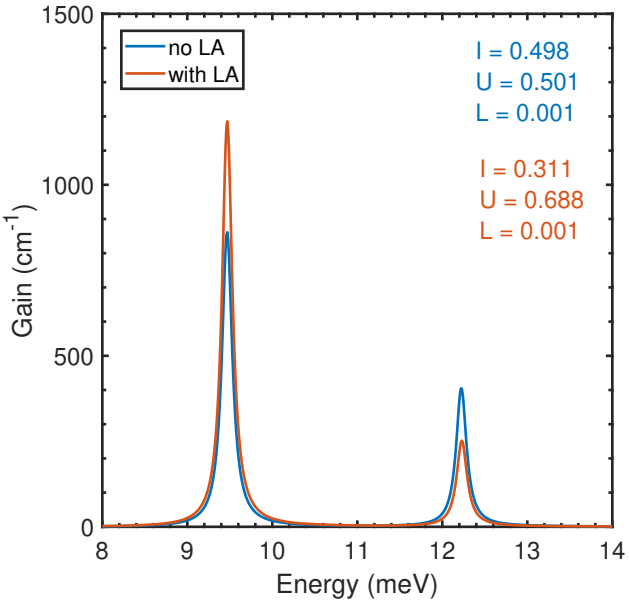

Figure 4.5: With / without LA phonons at T=0K, 16kV/cm. The populations for with and without LA phonons is indicated in the text. This is calculated in the limit of no optical field, using the method of Ref. [85].

resulting in varying amounts of Lamb shifts. The features in the gain curve are generally broader as well, due to the stronger phonon interactions.

Finally, the IV characteristic is shown in Figure 4.8, at 50K. The values are within the expected range. Previous literature have shown that the current density in these devices are orders of magnitude smaller than their quantum well counterpart. It also shows that there will be electrical instabilities/ electric field domains, in agreement with previous literature [79]. In practice, this design cannot be experimentally realized. The design electric field cannot be reached.

4.5.2 Modified Design

A modified design was tested, The well and barrier layers are, starting from the phonon well 21.3/3.7/10.7/3.8 nm of GaAs /$Al_{0.2}Ga_{0.8}As$. The band structure is shown in Figure 4.9. Compared to the original design, only the well lengths are widened. This is the same design strategy as proposed in Ref [34]. By widening the wells, the energy spacing between

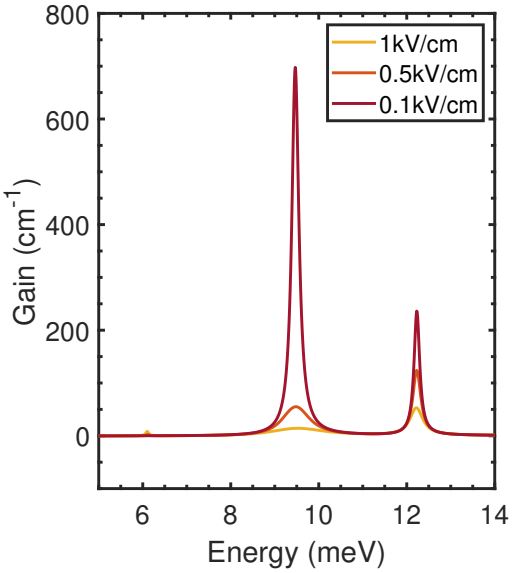

Figure 4.6: Gain spectra with increasing optical field strengths, calculated at 0K and 16kV/cm, with LA phonons.

the resonant states at the first IV peak (see Figure 4.10) is decreased to 26.5meV, away from the LO phonon energy. This results in smaller peak current density. The design electric field (9.2kV/cm) in this case can be experimentally realized.

The gain at 50K and 9.2kV/cm is shown in Figure 4.11. It features a relatively high peak gain of 600cm^{-1}, despite the energy difference between the upper and lower lasing states being close to the LO phonon energy. The maximum gain at 300K is around 57cm^{-1}. In comparison to other simulation results in the literature, it is within the expected range. For example T. Grange obtained around 20-30cm^{-1} at 300K for nanowire diameter around 50nm, however for a different material system and different design scheme. Burnett obtained order of 100cm^{-1} in the region of stability for his modified design at 300K.

4.6 Conclusions

This section has presented the work done on the modeling of QDCLs. A transport model in the Interaction picture or also known as Redfield equations has been derived and implemented. This model is intuitive, as one can deduce from it the semiclassical rate equations.

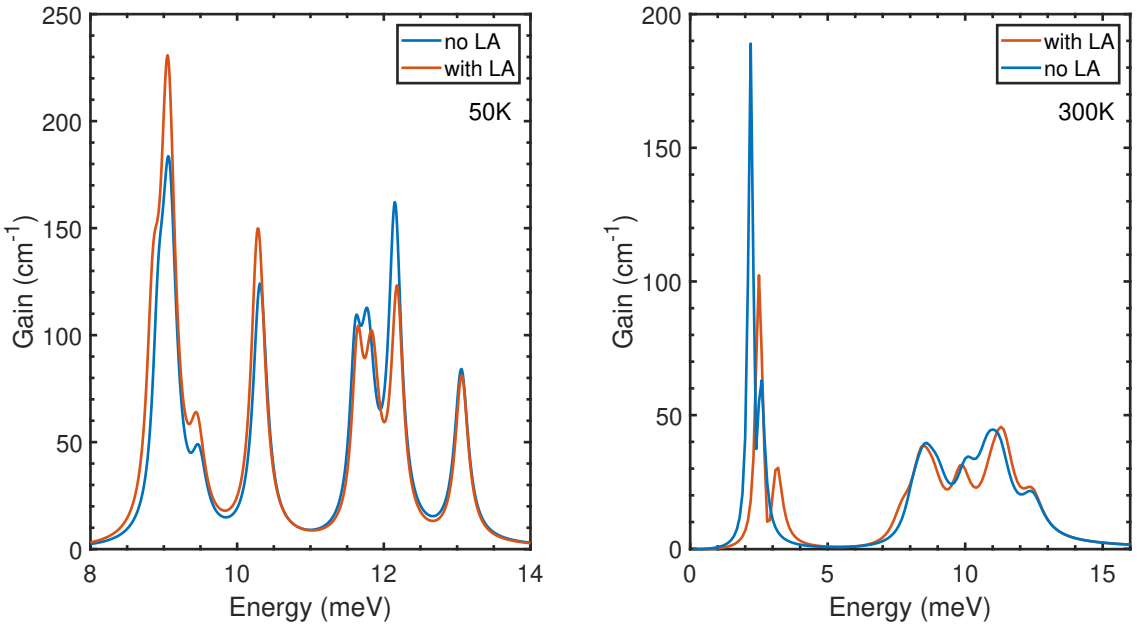

Figure 4.7: Gain spectra at 50K and 300K, for with and without LA phonons. At electric field of 16kV/cm, and is calculated in the limit of no optical field, using the method of Ref. [85].

It includes the periodicity in the QCL structure, and it is also general enough to be used on all different QCL designs. Scattering mechanisms included are the LO and LA phonons, however one can easily include other scattering mechanisms such as ionized impurities and interface roughness scattering as well.

The gain and IV were calculated for a two well design. This was based on traditional well based THz QCLs where the depopulation channel is tuned to the LO phonon energy. It was found that the LA phonons can help to inject carriers into the upper lasing state, at low temperatures. At temperature of 0K, this was an additional 0.187 amount of carriers injected into the upper lasing state. However, the design electric field cannot be experimentally reached in this particular quantum design due to early NDR issues, and the well layers were widened in order to overcome this problem. The range of values obtained for the gain (57cm^{-1} at 300K) and current density in this design are in agreement with previous literature.

Future work could include the addition of more scattering mechanisms such as ionized impurities and interface roughness. This would add additional dephasing and may help

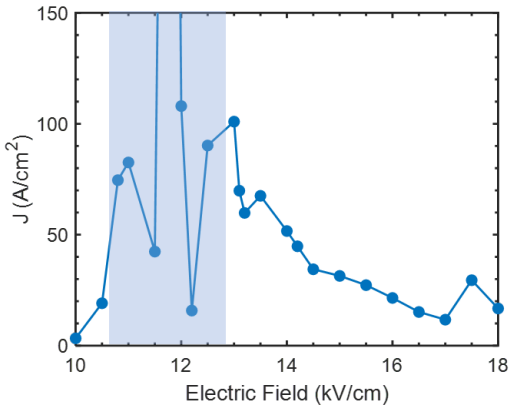

Figure 4.8: IV at 50K. Note however that the values calculated in the region shaded in blue are not reliable, because negative occupations were present in the results of the middle module for some of the data points.

with the numerics as well. The code could also be improved in terms of speed, which would be helpful when including more states and scattering mechanisms in the simulation.

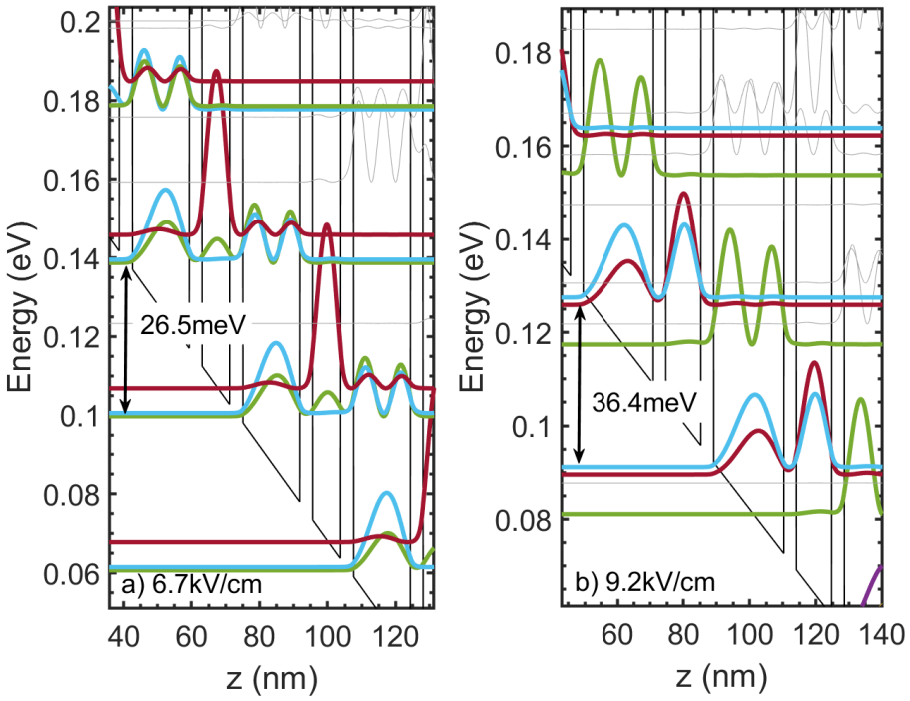

Figure 4.9: Band diagrams at a) 6.7kV/cm and b) 9.2kV/cm which are at the two resonances in the IV. The states included in the simulation are plotted in thick colored lines.

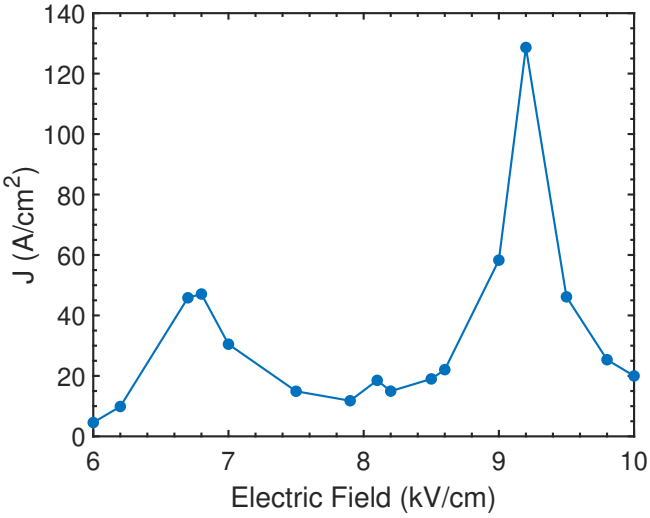

Figure 4.10: Simulated IV of the new design at 50K.

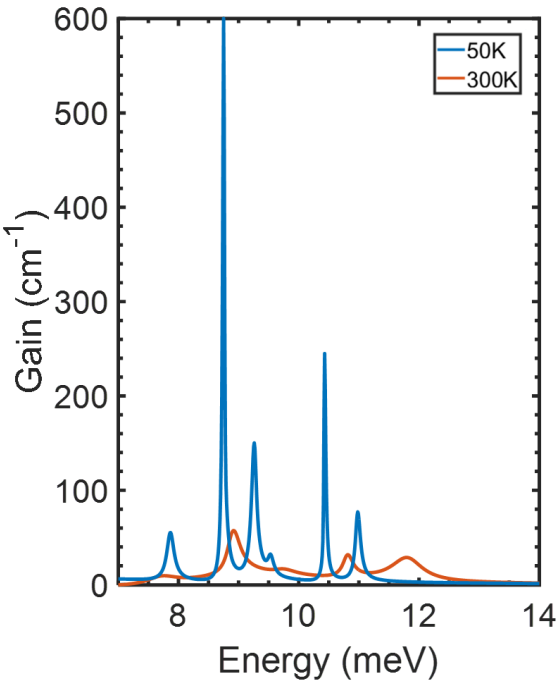

Figure 4.11: Gain at 9.2kV/cm for the modified design, at temperatures of 50K and 300K.

4.7 Appendix: Simulation Parameters

Table 4.2 lists the simulation parameters used in this Chapter.

Table 4.2: Parameters used for the QDCL structure.

Parameter	Expression/Value	Ref.
Electron effective mass of $Al_xGa_{1-x}As$ in units of m_0	$m_e(r,z) = 0.067 + 0.083x$	[89]
Conduction band offset	$0.65(1.36 + 0.22x)x$	[90]
Deformation potential	$D_c = -14.6\text{eV}$	[14]
Material density	$\rho_M = 5.37\text{g/cm}^3$	[14]
Speed of sound	$u_s = 4780\text{m/s}$	[14]
LO phonon energy	$\hbar\omega_{LO} = 36.7\text{meV}$	[91]
static permittivity	$\epsilon_s = 12.9\epsilon_0$	[91]
high frequency permittivity	$\epsilon_\infty = 10.9\epsilon_0$	[91]

Chapter 5

Conclusions

We are now in the second quantum revolution where we are designing the properties of optoelectronic devices using quantum mechanical principles. This thesis for a large part dealt with how the geometry of the QD affects its interactions with the environment, and by understanding this, one can engineer the desired properties.

For the interband part, this thesis developed the theory for the emission spectra from QDs in nanowires being broadened due to interactions with phonons. In addition to the well known Independent Boson model, which accounts for the broad phonon sidebands, the quadratic interaction due to both LO and LA phonons are also included. The theory is compared to experimental results, from which a good agreement with the general trends is found. Furthermore, structural and material variations in the simulation are performed. It was found that the linewidth broadening can range over three orders of magnitude due to the structural variations, which can tune the energy spacing(s) in resonance with the LO phonon energy. These are clearly important considerations for the design of future optoelectronic devices.

For the intersubband part, a quantum transport model was derived and implemented to simulate for the operation characteristics of a quantum dot cascade laser (QDCL). This model includes the periodicity, and uses a delocalized basis. This model is valid for intermediate to weak radial confinement strengths (roughly diameters greater than 40nm). Nevertheless this is even more so of experimental interest than the strong confinement regime – too small of a diameter would be difficult for fabrication, would encounter high surface currents, and low mechanical stability. It was found that at low temperatures, LA phonons assist the electron injection into the upper lasing state to obtain higher net gain. At higher temperatures this process is less significant due to the thermal backfilling. Sim-

ulation of the IV suggests strong early negative differential resistance issues, in accordance with previous literature. In order to circumvent this problem, a modified design scheme according to previous literature was investigated.

Future work could include speeding up all of the numerical codes developed in this thesis, which would involve interfacing with C/C++, as well as making use of high capability computational resources. On the theoretical side of things, one could add in more scattering mechanisms in the QDCL model. This additional dephasing would also help with the numerics.

In conclusion, theories have been presented to model the band structure and electron transport in quantum dots, with a focus on LO and LA phonon interactions. Trends between the QD geometry and its interband emission properties have been elucidated. In the intersublevel regime, with the continuous advancement of fabrication technologies, I am optimistic that this transport model will be useful for the design of QDCLs.

References

[1] R Tsu and Leo Esaki. Tunneling in a finite superlattice. Applied Physics Letters, 22(11):562–564, 1973.

[2] Leo Esaki and Ray Tsu. Superlattice and negative differential conductivity in semiconductors. IBM Journal of Research and Development, 14(1):61–65, 1970.

[3] MA Reed, JN Randall, RJ Aggarwal, RJ Matyi, TM Moore, and AE Wetsel. Observation of discrete electronic states in a zero-dimensional semiconductor nanostructure. Physical Review Letters, 60(6):535, 1988.

[4] Juan Marquez, Lutz Geelhaar, and Karl Jacobi. Atomically resolved structure of inas quantum dots. Applied Physics Letters, 78(16):2309–2311, 2001.

[5] Centre for Nanoscience and Nanotechnology. Qd group @ c2n. http://www.qdgroup.universite-paris-saclay.fr/modeling.html, 2020. Accessed 03/15/20.

[6] Michael E Reimer, Maarten P Van Kouwen, Maria Barkelid, Moira Hocevar, Maarten HM Van Weert, Rienk E Algra, Erik PAM Bakkers, Mikael T Björk, Heinz Schmid, Heike Riel, et al. Single photon emission and detection at the nanoscale utilizing semiconductor nanowires. Journal of Nanophotonics, 5(1):053502, 2011.

[7] Takeshi Suzuki, Rohan Singh, Galan Moody, Marc Aßmann, Manfred Bayer, Arne Ludwig, Andreas D Wieck, and Steven T Cundiff. Dephasing of inas quantum dot p-shell excitons studied using two-dimensional coherent spectroscopy. Physical Review B, 98(19):195304, 2018.

[8] Gerald D Mahan. Many-particle physics. Springer Science & Business Media, 2013.

[9] Birgit Krummheuer, Vollrath Martin Axt, and Tilmann Kuhn. Theory of pure dephasing and the resulting absorption line shape in semiconductor quantum dots. Physical Review B, 65(19):195313, 2002.

[10] Thomas Grange. Decoherence in quantum dots due to real and virtual transitions: A nonperturbative calculation. Physical Review B, 80(24):245310, 2009.

[11] Egor A Muljarov and R Zimmermann. Dephasing in quantum dots: Quadratic coupling to acoustic phonons. Physical review letters, 93(23):237401, 2004.

[12] T Takagahara. Theory of exciton dephasing in semiconductor quantum dots. Physical Review B, 60(4):2638, 1999.

[13] Greta Lindwall, Andreas Wacker, Carsten Weber, and Andreas Knorr. Zero-phonon linewidth and phonon satellites in the optical absorption of nanowire-based quantum dots. Physical review letters, 99(8):087401, 2007.

[14] Petru Tighineanu, Chris L Dreeßen, Christian Flindt, Peter Lodahl, and Anders S Sørensen. Phonon decoherence of quantum dots in photonic structures: broadening of the zero-phonon line and the role of dimensionality. Physical Review Letters, 120(25):257401, 2018.

[15] G Ortner, DR Yakovlev, M Bayer, S Rudin, TL Reinecke, S Fafard, Zbigniew Wasilewski, and A Forchel. Temperature dependence of the zero-phonon linewidth in in as/ ga as quantum dots. Physical Review B, 70(20):201301, 2004.

[16] S Rudin, TL Reinecke, and Manfred Bayer. Temperature dependence of optical linewidth in single inas quantum dots. Physical Review B, 74(16):161305, 2006.

[17] Paweł Machnikowski. Change of decoherence scenario and appearance of localization due to reservoir anharmonicity. Physical review letters, 96(14):140405, 2006.

[18] J Förstner, C Weber, J Danckwerts, and A Knorr. Phonon-assisted damping of rabi oscillations in semiconductor quantum dots. Physical review letters, 91(12):127401, 2003.

[19] S Weiler, A Ulhaq, SM Ulrich, D Richter, M Jetter, P Michler, C Roy, and Stephen Hughes. Phonon-assisted incoherent excitation of a quantum dot and its emission properties. Physical Review B, 86(24):241304, 2012.

[20] Ross Manson, Kaushik Roy-Choudhury, and Stephen Hughes. Polaron master equation theory of pulse-driven phonon-assisted population inversion and single-photon emission from quantum-dot excitons. Physical Review B, 93(15):155423, 2016.

[21] Ahsan Nazir and Dara PS McCutcheon. Modelling exciton–phonon interactions in optically driven quantum dots. Journal of Physics: Condensed Matter, 28(10):103002, 2016.

[22] A. Ulhaq, S. Weiler, C. Roy, S. M. Ulrich, M. Jetter, S. Hughes, and P. Michler. Detuning-dependent mollow triplet of a coherently-driven single quantum dot. Optics Express, 21:4382, 2013.

[23] Chris Gustin and Stephen Hughes. Pulsed excitation dynamics in quantum-dot–cavity systems: Limits to optimizing the fidelity of on-demand single-photon sources. Physical Review B, 98(4), jul 2018.

[24] F. Milde, A. Knorr, and S. Hughes. Role of electron-phonon scattering on the vacuum rabi splitting of a single-quantum dot and a photonic crystal nanocavity. Physical Review B, 78(3):035330, jul 2008.

[25] Antoine Reigue, Jake Iles-Smith, Fabian Lux, Léonard Monniello, Mathieu Bernard, Florent Margaillan, Aristide Lemaitre, Anthony Martinez, Dara PS Mccutcheon, Jesper Mørk, et al. Probing electron-phonon interaction through two-photon interference in resonantly driven semiconductor quantum dots. Physical review letters, 118(23):233602, 2017.

[26] Stefan Gerhardt, Jake Iles-Smith, Dara PS McCutcheon, Yu-Ming He, Sebastian Unsleber, Simon Betzold, Niels Gregersen, Jesper Mørk, Sven Höfling, and Christian Schneider. Intrinsic and environmental effects on the interference properties of a high-performance quantum dot single-photon source. Physical Review B, 97(19):195432, 2018.

[27] J. Iles-Smith, D. P. S. McCutcheon A. Nazir, and J. Mørk. Phonon scattering inhibits simultaneous near-unity efficiency and indistinguishability in semiconductor single-photon sources. Nat. Phot., 11:521–526, 2017.

[28] A Musial, A Marynski, P Mrowinski, J Andrzejewski, P Machnikowski, J Misiewicz, A Somers, S Hofling, JP Reithmaier, G Sek, et al. Phonon-assisted radiative recombination of excitons confined in strongly anisotropic nanostructures. Physical Review B, 90(12):125424, 2014.

[29] S Lüker, T Kuhn, and DE Reiter. Phonon impact on optical control schemes of quantum dots: Role of quantum dot geometry and symmetry. Physical Review B, 96(24):245306, 2017.

[30] R Ferreira, A Berthelot, T Grange, E Zibik, Guillaume Cassabois, and L Wilson. Decoherence effects in the intraband and interband optical transitions in inas/gaas quantum dots. Journal of Applied Physics, 105(12):122412, 2009.

[31] Masayoshi Tonouchi. Cutting-edge terahertz technology. Nature photonics, 1(2):97, 2007.

[32] Jerome Faist, Federico Capasso, Deborah L Sivco, Carlo Sirtori, Albert L Hutchinson, and Alfred Y Cho. Quantum cascade laser. Science, 264(5158):553–556, 1994.

[33] Rüdeger Köhler, Alessandro Tredicucci, Fabio Beltram, Harvey E Beere, Edmund H Linfield, A Giles Davies, David A Ritchie, Rita C Iotti, and Fausto Rossi. Terahertz semiconductor-heterostructure laser. Nature, 417(6885):156, 2002.

[34] Benjamin Adams Burnett. Design and modeling of high temperature terahertz quantum cascade lasers. PhD thesis, UCLA, 2016.

[35] Thomas Grange. Electron transport in quantum wire superlattices. Physical Review B, 89(16):165310, 2014.

[36] MI Amanti, A Bismuto, M Beck, L Isa, K Kumar, E Reimhult, and Jérôme Faist. Electrically driven nanopillars for thz quantum cascade lasers. Optics express, 21(9):10917–10923, 2013.

[37] Michael Krall, Martin Brandstetter, Christoph Deutsch, Hermann Detz, Aaron Maxwell Andrews, Werner Schrenk, Gottfried Strasser, and Karl Unterrainer. Subwavelength micropillar array terahertz lasers. Optics express, 22(1):274–282, 2014.

[38] Oliver Marquardt, Manfred Ramsteiner, Pierre Corfdir, Lutz Geelhaar, and Oliver Brandt. Modeling the electronic properties of gaas polytype nanostructures: Impact of strain on the conduction band character. Physical Review B, 95(24):245309, 2017.

[39] Maaike Bouwes Bavinck, Klaus D Jons, Michal Zielinski, Gilles Patriarche, Jean-Christophe Harmand, Nika Akopian, and Val Zwiller. Photon cascade from a single crystal phase nanowire quantum dot. Nano letters, 16(2):1081–1085, 2016.

[40] Curt A Flory, Charles B Musgrave, and Zhiyong Zhang. Quantum dot properties in the multiband envelope-function approximation using boundary conditions based upon first-principles quantum calculations. Physical Review B, 77(20):205312, 2008.

[41] Filippo Troiani, Ulrich Hohenester, and Elisa Molinari. Electron-hole localization in coupled quantum dots. Physical Review B, 65(16):161301, 2002.

[42] Kuniharu Takei, Hui Fang, S Bala Kumar, Rehan Kapadia, Qun Gao, Morten Madsen, Ha Sul Kim, Chin-Hung Liu, Yu-Lun Chueh, Elena Plis, et al. Quantum confinement effects in nanoscale-thickness inas membranes. Nano letters, 11(11):5008–5012, 2011.

[43] Paul Harrison and Alex Valavanis. Quantum wells, wires and dots: theoretical and computational physics of semiconductor nanostructures. John Wiley & Sons, 2016.

[44] Carsten Weber. Optical Dynamics in Low-Dimensional Semiconductor Heterostructures. Quantum Dots and Quantum Cascade Lasers. PhD thesis, Berlin Institute of Technology, 2008.

[45] Andreas Wacker. lattice vibration intro.

[46] Brews ohare. File:optical acoustic vibrations.png-wikimedia. https://commons.wikimedia.org/wiki/File:Optical_%26_acoustic_vibrations.png, 2012. Accessed 04/13/20.

[47] Matthias-René Dachner. Influence of phonons on light emission and propagation in semiconductor nano optics. Doctoral thesis, Technische Universität Berlin, Fakultät II - Mathematik und Naturwissenschaften, Berlin, 2013.

[48] Martijn Wubs, LG Suttorp, and Aart Lagendijk. Multiple-scattering approach to interatomic interactions and superradiance in inhomogeneous dielectrics. Physical Review A, 70(5):053823, 2004.

[49] H.P. Breuer, F. Petruccione, and S.P.A.P.F. Petruccione. The Theory of Open Quantum Systems. Oxford University Press, 2002.

[50] S. Mukamel. Principles of nonlinear optical spectroscopy. Oxford series in optical and imaging sciences. Oxford University Press, 1995.

[51] Gediminas Kiršanskas, Martin Franckié, and Andreas Wacker. Phenomenological position and energy resolving lindblad approach to quantum kinetics. Physical Review B, 97(3):035432, 2018.

[52] Simone De Liberato. Introduction to non-perturbative cavity quantum electrodynamics. https://www.youtube.com/watch?v=658LJtsnFk0, 2018. Accessed 01/02/20.

[53] Anders Nysteen. Cavity qed-engineering the phonon interactions. 2011.

[54] EA Muljarov and R Zimmermann. Exciton dephasing in quantum dots: Coupling to lo phonons via excited states. physica status solidi (b), 245(6):1106–1109, 2008.

[55] Egor A Muljarov and Roland Zimmermann. Exciton dephasing in quantum dots due to lo-phonon coupling: An exactly solvable model. Physical review letters, 98(18):187401, 2007.

[56] Chiranjeeb Roy. Quantum Theory of Phonon-mediated Decoherence and Relaxation of Two-level Systems in a Structured Electromagnetic Reservoir. PhD thesis, University of Toronto, 2009.

[57] AV Uskov, A-P Jauho, Bjarne Tromborg, Jesper Mørk, and R Lang. Dephasing times in quantum dots due to elastic lo phonon-carrier collisions. Physical review letters, 85(7):1516, 2000.

[58] Emil V Denning, Jake Iles-Smith, Niels Gregersen, and Jesper Mork. Phonon effects in quantum dot single-photon sources. Optical Materials Express, 10(1):222–239, 2020.

[59] Gabriele Bulgarini, Michael E Reimer, Tilman Zehender, Moïra Hocevar, Erik PAM Bakkers, Leo P Kouwenhoven, and Valery Zwiller. Spontaneous emission control of single quantum dots in bottom-up nanowire waveguides. Applied Physics Letters, 100(12):121106, 2012.

[60] Paola Borri, W Langbein, U Woggon, V Stavarache, D Reuter, and AD Wieck. Exciton dephasing via phonon interactions in inas quantum dots: Dependence on quantum confinement. Physical Review B, 71(11):115328, 2005.

[61] Paulo E Faria Junior, Tiago Campos, Carlos MO Bastos, Martin Gmitra, Jaroslav Fabian, and Guilherme M Sipahi. Realistic multiband k· p approach from ab initio and spin-orbit coupling effects of inas and inp in wurtzite phase. Physical Review B, 93(23):235204, 2016.

[62] Dan Dalacu, Khaled Mnaymneh, Jean Lapointe, Xiaohua Wu, Philip J Poole, Gabriele Bulgarini, Val Zwiller, and Michael E Reimer. Ultraclean emission from inasp quantum dots in defect-free wurtzite inp nanowires. Nano letters, 12(11):5919–5923, 2012.

[63] Amrit De and Craig E Pryor. Predicted band structures of iii-v semiconductors in the wurtzite phase. Physical Review B, 81(15):155210, 2010.

[64] M Beaudoin, A Bensaada, R Leonelli, P Desjardins, RA Masut, L Isnard, A Chennouf, and G L'Espérance. Self-consistent determination of the band offsets in in as x p 1- x/inp strained-layer quantum wells and the bowing parameter of bulk in as x p 1- x. Physical Review B, 53(4):1990, 1996.

[65] S Hughes, P Yao, F Milde, A Knorr, D Dalacu, K Mnaymneh, V Sazonova, PJ Poole, GC Aers, J Lapointe, et al. Influence of electron-acoustic phonon scattering on off-resonant cavity feeding within a strongly coupled quantum-dot cavity system. Physical Review B, 83(16):165313, 2011.

[66] NSM Archive. Optical properties of indium arsenide (inas). http://www.ioffe.ru/SVA/NSM/Semicond/InAs/optic.html, 2019. Accessed 05/01/19.

[67] NSM Archive. Basic parameters of indium arsenide (inas). http://www.ioffe.ru/SVA/NSM/Semicond/InAs/basic.html, 2019. Accessed 05/01/19.

[68] Ming Gong, Kaimin Duan, Chuan-Feng Li, Rita Magri, Gustavo A Narvaez, and Lixin He. Electronic structure of self-assembled in as/ in p quantum dots: Comparison with self-assembled in as/ ga as quantum dots. Physical Review B, 77(4):045326, 2008.

[69] VK Dixit, Sh D Singh, S Porwal, Ravi Kumar, Tapas Ganguli, AK Srivastava, and SM Oak. Determination of band offsets in strained inasxp1- x/inp quantum well by capacitance voltage profile and photoluminescence spectroscopy. Journal of Applied Physics, 109(8):083702, 2011.

[70] I Favero, Guillaume Cassabois, R Ferreira, D Darson, C Voisin, J Tignon, C Delalande, G Bastard, Ph Roussignol, and JM Gérard. Acoustic phonon sidebands in the emission line of single inas/gaas quantum dots. Physical Review B, 68(23):233301, 2003.

[71] Hussein M Ayedh and Andreas Wacker. Acoustic phonons in nanowires with embedded heterostructures. Journal of Nanomaterials, 2011:10, 2011.

[72] Martin A Kainz, Mykhaylo P Semtsiv, Georgios Tsianos, Sergii Kurlov, W Ted Masselink, Sebastian Schönhuber, Hermann Detz, Werner Schrenk, Karl Unterrainer, Gottfried Strasser, et al. Thermoelectric-cooled terahertz quantum cascade lasers. Optics express, 27(15):20688–20693, 2019.

[73] Lorenzo Bosco, Martin Franckié, Giacomo Scalari, Mattias Beck, Andreas Wacker, and Jérome Faist. Thermoelectrically cooled thz quantum cascade laser operating up to 210 k. Applied Physics Letters, 115(1):010601, 2019.

[74] EA Zibik, Thomas Grange, BA Carpenter, NE Porter, R Ferreira, G Bastard, D Stehr, S Winnerl, M Helm, HY Liu, et al. Long lifetimes of quantum-dot intersublevel transitions in the terahertz range. Nature materials, 8(10):803–807, 2009.

[75] A Wade, G Fedorov, D Smirnov, S Kumar, BS Williams, Q Hu, and JL Reno. Magnetic-field-assisted terahertz quantum cascade laser operating up to 225 k. Nature Photonics, 3(1):41–45, 2009.

[76] Yongquan Zeng, Guozhen Liang, Hou Kun Liang, Shampy Mansha, Bo Meng, Tao Liu, Xiaonan Hu, Jin Tao, Lianhe Li, Alexander Giles Davies, et al. Designer multimode localized random lasing in amorphous lattices at terahertz frequencies. Acs Photonics, 3(12):2453–2460, 2016.

[77] Elena Mavrona, Felice Appugliese, Johan Andberger, Janine Keller, Martin Franckié, Giacomo Scalari, and Jèrôme Faist. Terahertz refractive index matching solution. Optics express, 27(10):14536–14544, 2019.

[78] Nenad Vukmirović, Zoran Ikonić, Dragan Indjin, and Paul Harrison. Quantum transport in semiconductor quantum dot superlattices: Electron-phonon resonances and polaron effects. Physical Review B, 76(24):245313, 2007.

[79] Benjamin A Burnett and Benjamin S Williams. Density matrix model for polarons in a terahertz quantum dot cascade laser. Physical Review B, 90(15):155309, 2014.

[80] Alexander Mittelstädt, Ludwig A Th Greif, Stefan T Jagsch, and Andrei Schliwa. Room temperature lasing of terahertz quantum cascade lasers based on a quantum dot superlattice. arXiv preprint arXiv:1912.03988, 2019.

[81] Thomas Grange. Electron transport in quantum wire superlattices. Phys. Rev. B, 89:165310, Apr 2014.

[82] C Roy and S Hughes. Polaron master equation theory of the quantum-dot mollow triplet in a semiconductor cavity-qed system. Physical Review B, 85(11):115309, 2012.

[83] Rita C Iotti, Emanuele Ciancio, and Fausto Rossi. Quantum transport theory for semiconductor nanostructures: A density-matrix formulation. Physical Review B, 72(12):125347, 2005.

[84] M. Weissbluth. Photon-Atom Interactions. Elsevier Science, 2012.

[85] Andrew Pan, Benjamin A Burnett, Chi On Chui, and Benjamin S Williams. Density matrix modeling of quantum cascade lasers without an artificially localized basis: A generalized scattering approach. Physical Review B, 96(8):085308, 2017.

[86] Takeya Unuma, Masahiro Yoshita, Takeshi Noda, Hiroyuki Sakaki, and Hidefumi Akiyama. Intersubband absorption linewidth in gaas quantum wells due to scattering by interface roughness, phonons, alloy disorder, and impurities. Journal of applied physics, 93(3):1586–1597, 2003.

[87] David O Winge, Emmanuel Dupont, and Andreas Wacker. Ignition of quantum cascade lasers in a state of oscillating electric field domains. Physical Review A, 98(2):023834, 2018.

[88] S-C Lee, F Banit, M Woerner, and Andreas Wacker. Quantum mechanical wavepacket transport in quantum cascade laser structures. Physical Review B, 73(24):245320, 2006.

[89] NSM Archive. Aluminium gallium arsenide (algaas) - basic parameters. http://www.ioffe.ru/SVA/NSM/Semicond/AlGaAs/basic.html, 2020. Accessed 02/18/20.

[90] S. Adachi, Institution of Electrical Engineers, and INSPEC (Information service). Properties of Aluminium Gallium Arsenide. EMIS datareviews series. IEE, INSPEC, 1993.

[91] Razavipour, Seyed Ghasem. Design, analysis, and characterization of indirectly-pumped terahertz quantum cascade lasers, 2013.